A&A 517, A54 (2010)
DOI: 10.1051/0004-6361/200913366

Astronomy & Astrophysics

A deep survey of the AKARI north ecliptic pole field

I. *WSRT* 20 cm radio survey description, observations and data reduction

G. J. White[1,2], C. Pearson[2,3,1], R. Braun[4], S. Serjeant[1], H. Matsuhara[5], T. Takagi[5], T. Nakagawa[5], R. Shipman[6], P. Barthel[7], N. Hwang[8], H. M. Lee[9], M. G. Lee[9], M. Im[9], T. Wada[5], S. Oyabu[5], S. Pak[9], M.-Y. Chun[9], H. Hanami[10], T. Goto[11,8], and S. Oliver[12]

[1] Department of Physics and Astronomy, The Open University, Walton Hall, Milton Keynes, MK7 6AA, UK
e-mail: g.j.white@open.ac.uk
[2] Space Science and Technology Department, STFC Rutherford Appleton Laboratory, Chilton, Didcot, Oxfordshire, OX11 0QX, UK
[3] Institute for Space Imaging Science, University of Lethbridge, Lethbridge, Alberta, T1K 3M4, Canada
[4] CSIRO Astronomy and Space Science, Australia Telescope National Facility, CSIRO, Marsfield NSW 2122, Australia
[5] Institute of Space and Astronautical Science, JAXA, Yoshino-dai 3-1-1, Sagamihara, Kanagawa 229-8510, Japan
[6] SRON Netherlands Institute for Space Research, PO Box 800, 9700 AV Groningen, The Netherlands
[7] Kapteyn Astronomical Institute, University of Groningen, PO Box 800, 9700 AV Groningen, The Netherlands
[8] National Astronomical Observatory of Japan, Osawa, Mitaka, Tokyo 181-8588, Japan
[9] Astronomy Program, Department of Physics and Astronomy, Seoul National University, Seoul 151-747, Korea
[10] Physics Section, Faculty of Humanities and Social Sciences, Iwate University, Morioka 020-8550, Japan
[11] Institute for Astronomy, University of Hawaii, 2680 Woodlawn Drive, Honolulu, HI 96822, USA
[12] Department of Physics & Astronomy, School of Science and Technology, University of Sussex, Falmer, Brighton BN1 9QH, UK

Received 28 September 2009 / Accepted 26 April 2010

ABSTRACT

Aims. The Westerbork Radio Synthesis Telescope, *WSRT*, has been used to make a deep radio survey of an ∼1.7 degree^2 field coinciding with the AKARI north ecliptic pole deep field. The observations, data reduction and source count analysis are presented, along with a description of the overall scientific objectives.
Methods. The survey consisted of 10 pointings, mosaiced with enough overlap to maintain a similar sensitivity across the central region that reached as low as 21 μJy beam^{-1} at 1.4 GHz.
Results. A catalogue containing 462 sources detected with a resolution of 17.0″ × 15.5″ is presented. The differential source counts calculated from the *WSRT* data have been compared with those from the shallow *VLA – NEP* survey of Kollgaard et al. 1994, and show a pronounced excess for sources fainter than ∼1 mJy, consistent with the presence of a population of star forming galaxies at sub-mJy flux levels.
Conclusions. The AKARI north ecliptic pole deep field is the focus of a major observing campaign conducted across the entire spectral region. The combination of these data sets, along with the deep nature of the radio observations will allow unique studies of a large range of topics including the redshift evolution of the luminosity function of radio sources, the clustering environment of radio galaxies, the nature of obscured radio-loud active galactic nuclei, and the radio/far-infrared correlation for distant galaxies. This catalogue provides the basic data set for a future series of paper dealing with source identifications, morphologies, and the associated properties of the identified radio sources.

Key words. galaxies: active – radio continuum: galaxies – surveys – catalogs – cosmology: observations

1. Introduction

Deep radio and far-infrared (far-IR) surveys are useful to study the global properties of extragalactic source populations in the early Universe; to measure the evolution of AGN's and starburst galaxies at early epochs; and to understand the cosmic history of star formation. Recently, the Japanese AKARI infrared satellite has made deep surveys close to the north and the south ecliptic poles. These regions have relatively low line of sight extinction (to the distant Universe) and low hydrogen column densities, which are important if objects at large distances are to be detectable at optical and infrared wavelengths. To support the AKARI north ecliptic pole (*NEP*) survey (Matsuhara et al. 2006; Wada et al. 2008), this region has been observed using the Westerbork Radio Synthesis Telescope (*WSRT*).

The observational results of the *WSRT – AKARI – NEP* survey will be presented in three papers: a) the present paper presents the basic radio survey, source catalogues, radio source counts and statistics; b) a second paper will report the results from cross-correlation between the *WSRT* radio observations and the infrared source catalogue from the AKARI NEP survey; and c) the third paper will present optical identifications from a cross-correlation between the *WSRT* radio survey and deep optical imaging made using the Canada France Hawaii 3.6 m (CFHT) and SUBARU 8 m telescopes, and will address the more global objectives of the survey stated above.

2. Multi-wavelength observations

The two ecliptic poles are amongst the deepest exposure regions that have been observed by many infrared satellite missions, and provide a wealth of data about the distant source populations, for example the surveys of IRAS (Hacking et al. 1987; Aussel et al. 2000), ISO (Stickel et al. 1998; Aussel et al. 2000), COBE (Bennett et al. 1996), and ROSAT (Mullis et al. 2001, 2003). Other surveys of this region at radio wavelengths have been made with the *VLA* (Kollgaard et al. 1994; Brinkmann et al. 1999, at 20 and 91 cm); Westerbork: Rengelink et al. (1997); Effelsberg 100 m telescope (Loiseau et al. 1988); and in 2.7 GHz surveys by Condon & Broderick (1985, 1986) and Loiseau et al. (1988); at optical/IR wavelengths (Gaidos et al. 1993; and Kümmel et al. 2000, 2001); and at X-ray wavelengths using ROSAT by Henry et al. (2001) and Mullis et al. (2001). The area around the *NEP* has a moderate/low level of HI emission $\sim 4.3 \times 10^{20}$ cm^{-2} (Elvis et al. 1994). This corresponds to a line of sight extinction $A_v \sim 0.2$–0.5 mag, favouring very deep optical and near-infrared observations because of the low level of foreground extinction (Zickgraf et al. 1997). Optical and infrared surveys provide key information to help to understand the source populations of the *NEP* region, in particular the AKARI mission and its supporting ancillary programmes have included two deep 2.4–24 μm wavelength surveys at the North Ecliptic Pole (*NEP*): a) covering a 0.4 deg^2 circular area (known as *NEP*-Deep – see Matsuhara et al. 2006); and b) a wide and shallow 2.4–24 μm survey covering a 5.8 deg^2 circular area surrounding the *NEP*-Deep field (also known as *NEP*-Wide – Lee et al. 2009).

Optical, radio, X-ray and infrared surveys provide essential support to the interpretation of deep extragalactic radio surveys. A shallow *VLA* 20 cm survey of the *NEP* region was made by Kollgaard et al. (1994), which covered an area of 29.3 deg^2. The Kollgaard survey reported 2435 radio sources with flux densities ranging from 0.3–1000 mJy, observed with a 20″ beam and 1σ noise ~60 μJy per beam at the centre of the survey field. A comparison between this radio survey and the NASA Extragalactic database, and with other catalogues (including the ROSAT X-ray catalogue), resulted in the identification of ~20% of the sources, with ~6% of the sources found to be extended with diameters ≥30″. A 2.7 GHz survey of the region was made by Condon & Broderick (1985, 1986). Between 1 and 150 mJy, the slope of the log N − log S relationship was 0.68 ± 0.03. An even larger area of 570 degrees^2 was observed at 325 MHz using the *WSRT* telescope by Rengelink et al. (1997) in the *WENSS* survey (beam size 54″), which resulted in the detection of more than 11 000 sources. The source populations have already in this region include galaxy clusters (Gioia et al. 2003, 2004; Hwang et al. 2007; Goto et al. 2008), radio galaxy clusters (Branchesi et al. 2006), stars (Pretorious et al. 2007; Micela et al. 2007; Affer et al. 2008), X-ray sources (Voges et al. 2001; Henry et al. 2001, 2006) and infrared sources (Kümmel et al. 2000).

3. *WSRT* Observations

The radio observations presented in this paper were observed during 2004 with the *WSRT* operated at 20 cm wavelength. The array included fourteen 25 m telescopes arranged in a 2.7 km east-west configuration, with signals processed using a digital continuum 2-bit back end consisting of eight 20 MHz bandwidth sub-bands across the frequency range 1301–1461 MHz. The *NEP* observations were interleaved with observations of the intensity, polarisation and phase calibration sources 3C 147 and 3C 286, which past experience suggested should lead to a flux density calibration accuracy of better than 5%. The survey mosaic was made from 10 discrete pointings that were positioned on an hexagonal grid, with beam spacings at the 70% point of the 36.2′ primary beam full width half maximum (FWHM) diameter, each observed as a full 12 h track. This observing strategy was adopted to provide a relatively uniform noise background of less than ±10% over the most sensitive part of the surveyed area (see Prandoni et al. 2006) for a full treatment of mosaicing strategies, who show that this results in mosaiced noise variations of ≤5%), where a 1σ source detection sensitivity of point sources as low as 21 μJy per beam was achieved. The J2000 coordinate system is used throughout this paper. Experience at the WSRT suggests that the interpolation and coplanarity (also known as faceting) processing in the mosaicing step should not introduce errors in excess of 0.1 arcsec for a relatively small mosaic of this size.

The observations were reduced and calibrated using standard tasks in the *AIPS* software package. The data sets were uniformly of high quality, with only a few percent of the visibilities having to be flagged out, mostly due to low level radio interference. Each pointing was mapped onto a regular grid with 4″ pixels using a multi-frequency synthesis approach to minimise bandwidth smearing. Adjacent pointings were co-added to the FWHM point (Condon et al. 1998; Huynh et al. 2005). After a first iteration, model components with a flux density of more than ~1 mJy beam^{-1} were used for phase and amplitude self-calibration, to correct for residual phase and amplitude errors. The data were then re-imaged and cleaned with ~2000 clean components, at which point the side lobes of most of the strong sources were found to be below the noise level. There was however a particular problem toward the central position in the mosaic where the prominent galactic planetary nebula, the Cat's Eye Nebula (NGC 6543) lies close to the field centre. Since this is slightly extended at radio wavelengths, it presented a particular challenge to the data reduction and cleaning, and ultimately limited the rms noise level achievable in the immediate vicinity to be several times the thermal limit. However, the number of pixels affected was very small (≤0.1% of the total), and a correction for this was made during the differential source count calculation presented in Sect. 7.

After reduction of the individual pointings, the maps were individually intensity corrected using a model of the primary beam, and then mosaiced together into a final image using the *AIPS* task *LTESS*, to make a linearly combined mosaic, correcting for the individual primary beam patterns, and optimizing the signal to noise ratio. The pixels at the edges of the mosaiced region have higher noise uncertainties compared to those at the centre of the merged field because of the primary beam profile, and the mosaicing strategy. The mosaiced, primary beam corrected image of the high sensitivity region of the *WSRT* image is shown in Fig. 1.

Several automated source extraction and cataloging routines were tested, including the *AIPS* task *SAD* and the *MIRIAD* tasks *IMSAD* and *SFIND* (Sault et al. 1995), but the latter task was eventually adopted as the extraction task of choice for reasons that will be discussed in Sect. 4. A quantitative comparison between *SFIND*, *SAD*, *IMSAD*, and *SEXTRACTOR* has already been presented by Hopkins et al. (2002) to which the reader is referred for a rigorous treatment of noise and error estimates relevant to this paper.

The final restored beam size in the mosaic after all of the associated processing steps was 17.0″ × 15.5″ at position angle 0 degrees. The most sensitive part of the survey field had a 1σ rms sensitivity of 21 μJy beam^{-1} in the centre of the map,

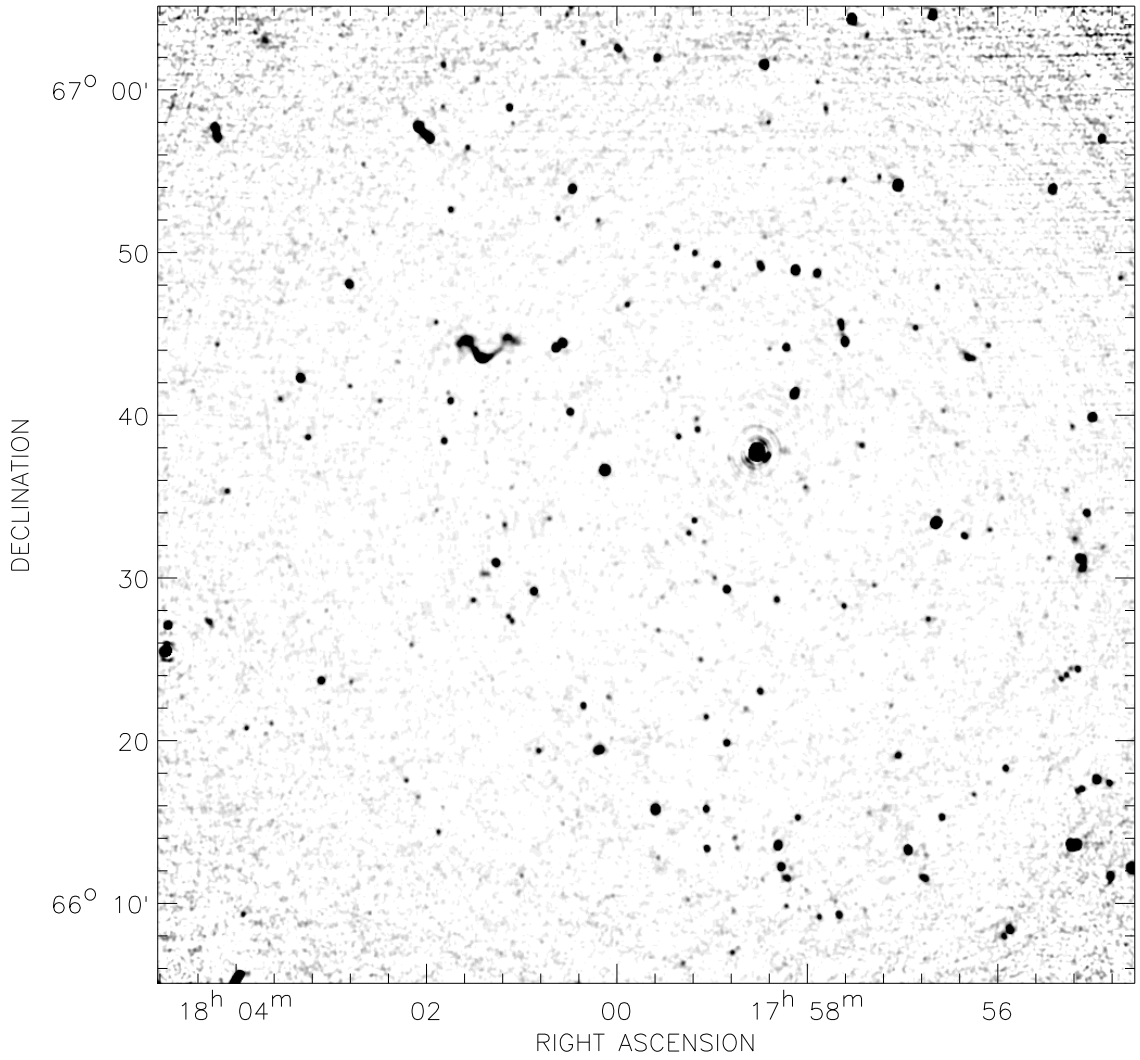

Fig. 1. The central 1 square degree area of the *WSRT* 20 cm map, corrected for the primary beam of the antenna. The bright Cats Eye Nebula lies ~5′ to the right of the centre of the map, where some faint residual sidelobe structure can be seen as part of a circular arc. The local noise levels are slightly elevated close to this source.

increasing to ≥100 μJy beam^{-1} toward the edges of the field, because of the primary beam attenuation correction. It was therefore not possible to use the same detection threshold across the whole of the mosaiced region. Furthermore, flux densities measured toward the image edges were increasingly affected by uncertainties in the primary beam model, and consequently the image analysis was restricted to those sources which lie in regions where the theoretical sensitivity is below 60 μJy beam^{-1} for noise considerations, and to mitigate other biases such as bandwidth smearing so as not to affect the source intensities by more than a few percent. To measure the noise, estimates of the rms errors were estimated using *SEXTRACTOR*, and separately using the *MIRIAD* task *SFIND*. The detection sensitivity is shown in Fig. 2, with similar results being obtained in *SEXTRACTOR* and in *SFIND*.

4. Source catalogue

The *NEP* mosaic has a non-uniform and continuously varying noise level, a complex mosaicing strategy, and locally elevated noise levels around the few bright sources such as the Cat's Eye Nebula, and it is clear that source detection using an uniform flux threshold over the whole primary beam corrected image is not the optimal approach. Source detection in this case is better determined using locally determined noise levels – an approach that has already been used in other studies to improve the efficacy of their source detection catalogues (e.g. Morganti et al. 2004).

The source catalogue in this paper was built using the *MIRIAD* task *SFIND*. This is a method for identifying source pixels, where the detected sources are drawn from a distribution of pixels with a robustly known chance of being falsely drawn from the background (see Hopkins et al. 1999, 2002; and Morganti et al. 2004) for a complete description justifying the adoption of this technique. *SFIND* robustly characterises the fraction of expected pixels more rigorously than from a traditional sigma-clipping criterion – which is known to suffer limitations at lower signal-to-noise levels. Noise estimation is implemented in the image plane by dividing the image into small square regions within which the mean and rms noise level are estimated by fitting a Gaussian to the pixel histogram in each region. The image is then normalised by subtracting the mean and dividing by the rms within each region, resulting in an image where pixel values are specified in units of the local rms noise level σ. *SFIND* uses a statistical technique, the false discovery rate (FDR), which assigns a threshold based on an acceptable

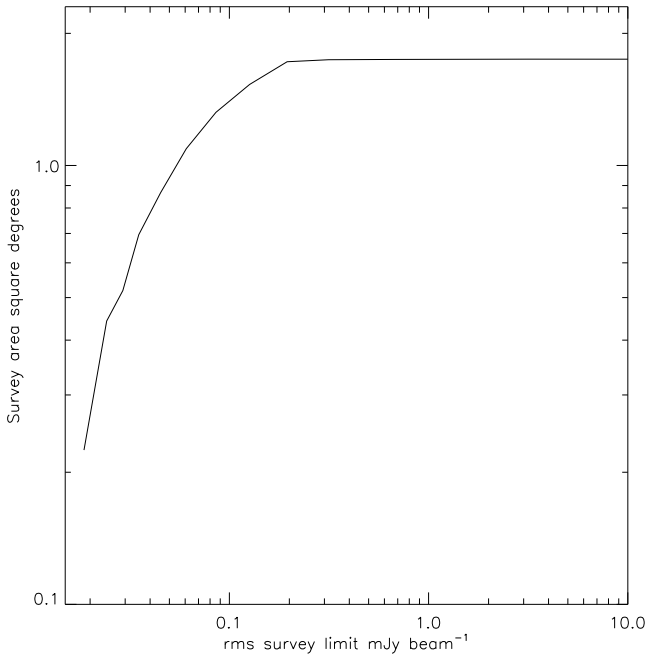

Fig. 2. The horizontal axis shows the typical 1σ noise level radially averaged as a function of the (vertical axis) total areal coverage.

rate of false detections (Hopkins et al. 2002). We followed Hopkins et al. (2002) by adopting an FDR value of 2%. Each of the sources identified by *SFIND* were visually inspected to remove any obvious mis-identifications. Comparison with independent catalogues derived using the *MIRIAD* task *IMSAD* (with a 7σ clip), and with one derived using *SEXTRACTOR* with a locally defined background rms were almost identical with the *SFIND* catalogue.

A sample from the final source catalogue is presented in Table 1.

The positional accuracy listed in the Table 1 is relative to the self-calibrated and bootstrapped reference frame described in Sect. 3, after mitigating the various effects mentioned above. Several other effects that can affect the positions include the mosaicing process (which we have discussed in Sect. 3; the signal-to-noise of the detected sources (presented in Table 1; and other observational effects that bias the positions or sizes of sources, which are discussed in Sect. 5. We also present an estimate of source dimensions estimated by deconvolving the measured sizes from the synthesized beam, reporting those more than double the synthesised beam size. Although is possible to model the source sizes in a more exact way (for example following the approach of Oosterbaan (1978), we only use the present source size data as a guide to whether the sources are either extended, or likely to be multi-component sources. A more detailed discussion of the WSRT source sizes will be made in a future paper that combines the present data set with higher resolution observations of the *NEP* field with the GMRT Telescope (Sedgwick et al. 2009). To test the accuracy of the radio reference frame, WSRT sources with a peak signal to noise ratio $\geq$10 which could be identified with compact optical galaxies from a deep SUBARU image (referenced from HST Guide Star positions) were found to have positional offsets within $\sim 2''$ of each other, randomly distributed around the nominal radio position. Further quantitative discussion of the optical identifications, and the radio-optical frame registration determined from a larger selection of optically identified sources will be presented in Paper 2, which is dedicated to the optical/infrared identifications from this survey (White et al., in preparation).

5. Flux accuracy and error estimates

The observations from a radio synthesis array must be corrected for various instrumental effects: a) the primary beam response of the antenna elements; b) time-average smearing due to the finite integration time; c) chromatic aberration resulting from the finite bandwidth (Bridle & Schwab 1989; Cotton 1989); and d) incompleteness at low signal to noise levels. We briefly describe the approach we have taken, below.

5.1. Time-average smearing

The data were observed using integration times of 60 s, which was estimated to lead to a reduction in the flux of point sources of no more than $\sim$1% for a point source $10'$ from the field centre, and it is believed that this does not play a dominant effect in determining source sizes.

5.2. Chromatic aberration

To correct for bandwidth smearing, the radio analog of optical chromatic aberration, we inserted 500 artificial point source models into the *uv*-data with peak values from $5-50\sigma$ using the *AIPS* task *UVCON*. This data were processed in a similar way to the *NEP* field, and *SFIND* was used to recover the source intensities and measure the noise uncertainties. There was no evidence significant variation of the source intensities with position in the mosaic, which is similar to the conclusion of Prandoni et al. (2000b) for a similar set of *ATCA* data.

5.3. Clean bias

Radio surveys can be affected by a "clean bias" effect, where a systematic under estimation of the peak and total source fluxes (Becker et al. 1995; White et al. 1997; Condon et al. 1998) is a consequence of redistribution of the flux from point sources to noise peaks in the image. Prandoni et al. (2000a,b) show that it is possible to mitigate this bias if the *CLEAN*ing process is stopped well before the maximum residual flux has reached the theoretical noise level. Following Garrett et al. (2000), we set the cleaning limit at 5 times the theoretical noise to mitigate against this effect.

5.4. Resolution bias

Resolution bias is an effect in which the peak flux densities of weak extended sources fall below the chosen detection limit, yet still have total integrated flux densities that are above the survey limit. In other studies, a 3% correction was required for source counts below 1 mJy (Moss et al. 2007; Garn et al. 2008), although no resolution correction was applied to brighter sources. This effect reduces the number of faint sources in differential source counts (see for example Hopkins et al. 2002), and we do not consider that it has a significant effect on our data reduction methodology.

5.5. Eddington bias

Since the source counts rise strongly with decreasing flux density, more sources will have their true fluxes "boosted" by the

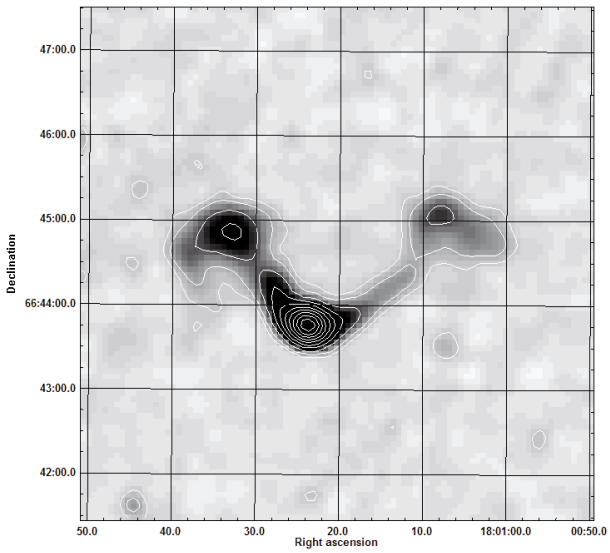

Fig. 3. The extended radio source centred on the $S_{\rm peak}$ = 12.3 mJy source NEP180123+664346. The contours are spaced at square root intervals for display purposes with the lowest level at 0.00010, and subsequent levels at 0.00023, 0.00063, 0.00129, 0.00222, 0.00342, 0.00488, 0.00661, 0.00861, 0.01086, 0.0122 Jy beam^{-1}. The two jets are strongly bent, suggesting that the source is moving through a relatively dense medium, such as that associated with a galaxy cluster.

effect of noise, than those that are "reduced" at higher flux densities (see discussion in Coppin et al. 2006). To examine the effect of this, a population of "test" point sources were added into a single field, uncorrected for the primary beam response using the *AIPS* task "*UVMOD*", and processed and extracted in the same way as the un-mosaiced survey data, with the difference between the detected counts, and those inputs, providing an estimate of the net amount of up-scattering. The effect of this was only significant in the lowest flux bin, and led to an overestimate of the source count by 16% (the boundaries of the lowest flux bin were ∼5% above the formal survey limit. This value should be compared with the value estimated by Moss et al. (2007) of 21%, which goes slightly closer to their formal survey limit. Consequently in later analysis the counts in the lowest flux bin (110−125 μJy were "de-boosted" by 16%. This correction has a negligible effect for fluxes above this limit, and it is safe to ignore it.

5.6. Component extraction

In the terminology of this paper a radio component is described as a region of radio emission represented by a Gaussian shaped object in the map. Close radio doubles are represented by two Gaussians and are deemed to consist of two components, which make up a single source. A clear case of a very extended radio source is shown in Fig. 3, and a selection of other sources with multiple components is shown in Fig. 4.

5.7. Resolved sources

Although it may seem relatively straightforward to calculate the density of sources as a function of the flux density, the distribution of angular sizes as a function of the flux density may also bias the results. It was assumed that the median sizes below 1 mJy remain approximately constant as a function of the flux density with those at higher flux levels. Fomalont et al. (2006) find that 8 ± 4% of the μJy sources have sizes greater than 4″. For low signal-to-noise ratio detections, Gaussian fitting routines may be significantly affected by noise spikes, leading to errors in the estimated widths and flux densities of the sources (Moss et al. 2007). This is one of the reasons for adopting the *SFIND* source extraction methodology in this paper. The ratio $S_{\rm total}/S_{\rm peak}$ = $(\theta_{\rm min}\ \theta_{\rm maj})/(b_{\rm min}\ b_{\rm maj})$ where $\theta_{\rm min}$ and $\theta_{\rm maj}$ are the major and minor axes of the detected source and $b_{\rm min}$ and $b_{\rm maj}$ are the major and minor axes of the restoring beam. The flux density ratio may be used to discriminate between unresolved sources and those which are much larger than the beam (see Prandoni et al. 2006). In Fig. 5, the ratio of the flux densities to the signal-to-noise ratio ($S_{\rm peak}/\sigma_{\rm local}$) is plotted for all sources above a 6σ local threshold. The biases introduced by using different thresholds have been modelled by Prandoni et al. (2000a,b), Owen et al. (2008) and Fomalont et al. (2006), which suggest that the biases are most prevalent below an ∼5−6σ (sigma-clip) threshold. To identify sources for which $S_{\rm total}/S_{\rm peak} < 1$, a functional form of the curve $f(x) = 1.0 \pm 3.22/x$ was plotted in Fig. 5 to define the point where 90% of the ≥6σ detections with $S_{\rm total}/S_{\rm peak} < 1$ lie above the curve (this is similar to the ratio adopted by Prandoni et al. 2000a,b). Reflecting this curve about $S_{\rm total}/S_{\rm peak} = 1$ shows those sources which lie between the two curves, and which are considered to be unresolved.

In Fig. 5 the flux ratio is shown as a function of the signal-to-noise for all the sources (or source components) in the *NEP* catalogue.

The flux density ratio shows a skewed distribution, where the tail toward high flux ratios is due to the presence of extended sources. Values for $S_{\rm total}/S_{\rm peak} < 1$ result from the effect of noise in affecting the source sizes (see Sect. 4). To establish a criterion for extension, such noise errors have to be taken into account. The lower envelope of the flux ratio distribution (the curve containing 90% of the sources) was determined, and mirrored it on its side (upper envelope in Fig. 5), so that unresolved sources should lie below the upper envelope. The upper envelope can be characterised by the equation from Huynh et al. (2005) that was found to characterise the 90% envelope of sources where $S_{\rm total} \leq S_{\rm peak}$, and a 5$\sigma$ cut off to the peak fluxes was adopted:

$$\frac{S_{\rm total}}{S_{\rm peak}} = 1 + \left[\frac{10}{\left(S_{\rm peak}/\sigma_{\rm fit}\right)^3}\right]. \quad (1)$$

It is worth noting that the envelope does not converge to unity at large signal-to-noise values. This is due to the radial smearing effect which systematically reduces the "peak" fluxes, leading to larger $S_{\rm total}/S_{\rm peak}$ ratios. From Fig. 5 we estimate the smearing effect to be 8% on average for the WSRT data (a similar effect has been reported by Prandoni et al. (2000a,b) comparing *ATCA* and *VLA* data in an overlapping field, where they report applying a 5% correction to their data). The fluxes in the table have been corrected for these effects as described in Sect. 5.11.

Radio sources are often made up of multiple components, as seen earlier in Fig. 4. The source counts need to be corrected for this, so that the fluxes of physically related components are summed together, rather than being treated as separate sources. Magliocchetti et al. (1998) have proposed criteria to identify the double and compact source populations, by plotting the separation of the nearest neighbour of a source against the summed flux of the two sources, and selecting for objects where the ratio of their fluxes, f_1 and f_2 is in the range $0.25 \leq f_1/f_2 \leq 4$. In Fig. 6 the sum of the fluxes of nearest neighbours are plotted against their separation.

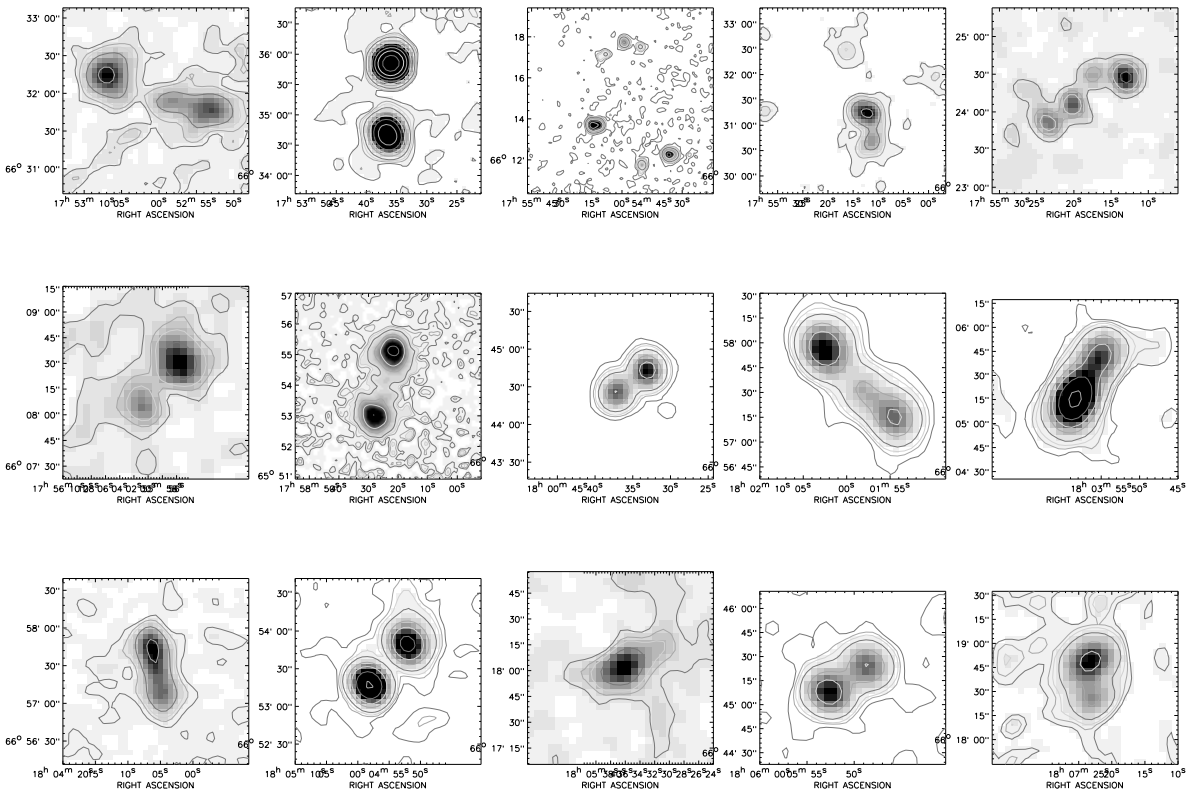

Fig. 4. Regions showing complex or extended structure. The vertical scale is Declination. The contours are at 0.0001, 0.0003, 0.0005, 0.001, 0.003, 0.006, 0.012, 0.024, 0.048 and 0.096 Jy beam^{-1} respectively.

The dashed line marks the boundary satisfying the separation criterion defined by Huynh et al. (2005):

$$\theta = 100 \left[\frac{S_{\rm total}({\rm mJy})}{10} \right]^{0.5} \quad (2)$$

where θ is in arc seconds. The 82 radio components in the present survey (i.e. 18% of the 462 catalogued entries) should be considered to be a part of double or multiple sources, and this will be taken account of in the differential source counts discussed later. A further correction for the incompleteness due to extended sources (Windhorst et al. 1993; Bondi et al. 2003) was considered, but found to have a negligible effect on the final catalogue, because of the relatively large beam in the present survey.

5.8. Positional accuracy

Noise fluctuations limit the rms positional uncertainty in each of the fitted sky coordinates (ΔRA or ΔDec) of a faint point source with an rms brightness fluctuation σ and FWHM resolution θ to (following Rengelink et al. 1997):

$$\sigma_p \approx \frac{\sigma\theta}{2S_{\rm peak}} \cdot \quad (3)$$

The positions listed in the Table 1 are those estimated from the external calibration sources and are internally consistent within Table 1. Further discussion of the positional alignment to the optical and infrared reference planes will be given in the second paper of this series.

5.9. Noise flux accuracy

The accuracy of flux estimates in radio interferometer data has been discussed by a number of authors, for example Rengelink et al. (1997). The accuracy of flux recovery with specific reference to the *SFIND* technique adopted for this paper has been presented in Hopkins et al. (2003), and will not be repeated in detail here. However, for completeness, we will repeat the Hopkins et al. (2003) equations using the terminology in the present paper, which reduce to those presented by Rengelink et al. (1997). For point sources, Hopkins et al. (2003) show that the total relative uncertainty in the integrated flux density is given by:

$$\frac{\sigma_{S_{\rm total}}}{S_{\rm total}} = \sqrt{2.5\frac{\sigma^2}{S_{\rm total}^2} + 0.01^2}. \quad (4)$$

The reader is referred to the papers listed above for more detailed analysis of this, where the treatments of both papers reduce to similar relationships for both extended and for point sources.

5.10. Comparison with the VLA flux density scaling

We initially compared the WSRT radio fluxes with those reported in the Kollgaard et al. (1994) paper. This showed that the *WSRT* fluxes below ~10 mJy appear to be too bright, initially giving some concern about the calibration efficacy of the *WSRT* data compared to Kollgaard's survey. However, from comparison between the integrated fluxes of the Kollgaard et al. (1994) survey and the NVSS catalogue, it appears that the former study may systematically overestimate the radio fluxes below about 10 mJy, as shown in Fig. 7.

It therefore appears that the Kollgaard et al. (1994) fluxes may be unreliable in the flux range appropriate to the *WSRT*

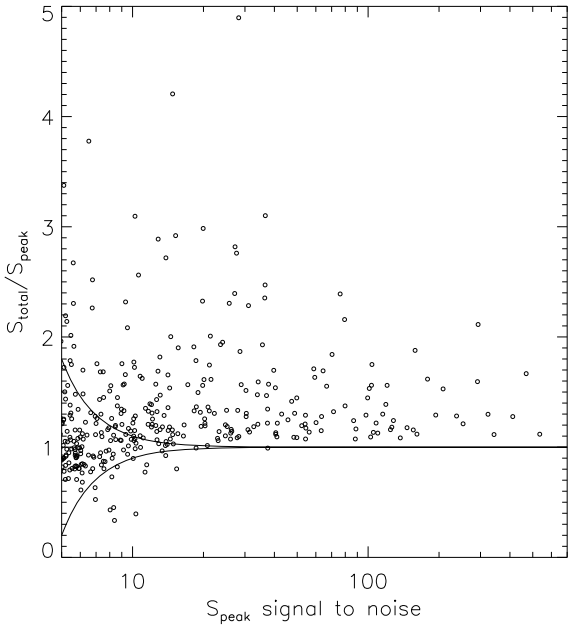

Fig. 5. Ratio of the integrated flux $S_{\rm total}$ to the peak one $S_{\rm peak}$ as a function of the source signal-to-noise. The lower and upper envelopes (dashed lines) of the flux ratio distribution are shown, along with small dots showing the unresolved sources, and larger filled circles indicating extended sources. It is likely that one of the measurements of $S_{\rm total}$ or $S_{\rm peak}$ where $(S_{\rm total}/S_{\rm peak}) < 1$, have been affected by noise, to the extent that the value of the ration is below unity – which mainly happens for the weaker sources.

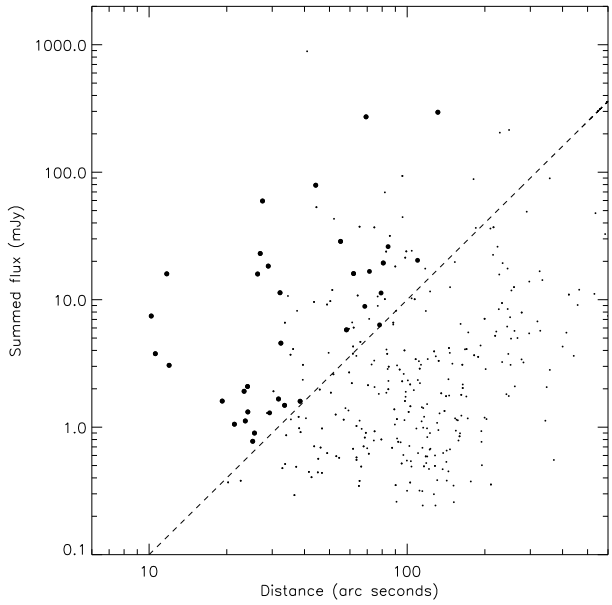

Fig. 6. This figure shows the sum of the flux densities of the nearest neighbours between sources from the detection catalogue. Following Magliocchetti et al. (1998) near neighbour pairs to the left of the line are considered as possible double sources. The double sources can be further constrained by adding the second constraint that the fluxes of the two components f_1 and f_2 should be in the range $0.25 \leq f_1/f_2 \leq 4$, and those sources satisfying this criterion are shown as bold circles in the figure, in other words the multiple component sources, with unhighlighted points representing single component sources.

survey, and that we should instead rely on NVSS fluxes to assess the efficacy of the present data.

To consider whether the differential source plots are affected by an incorrectly applied completeness correction, or are truly representative of astrophysical the source populations, such as an under-density of sources, or showing evidence for cosmic variance or clustering, we carried out a further series of tests. Firstly, a comparison was made between the fluxes of sources in common between the *VLA* and *WSRT* observations is shown in Fig. 8.

To check the efficacy of the *WSRT NEP* data, the flux densities of components measured in the *WSRT* survey were compared with those reported by Kollgaard et al. (1994), as shown in Fig. 8.

The two plots show reasonably good agreement between the two independent data sets, with the *VLA* peak fluxes of Kollgaard et al. (1994) systematically lying a little above the *WSRT* peak fluxes above ∼50 mJy, but being consistent with the *WSRT* fluxes below that. For the integrated fluxes, there is some evidence that the *WSRT* fluxes are systematically higher than the *VLA* fluxes by ∼2−30% at fluxes below 20 mJy, although consistent at higher flux densities. It is difficult to directly compare these, because of the different observational characteristics, and data reduction steps, and there is no a priori reason to favour one calibration over another. However, this test does show that at least at the level of a few tens of percent, and down to ∼1 mJy, the two data sets are broadly consistent with each other. It is however difficult to know whether or not this holds at lower flux densities, because of the lack of the lower sensitivity of the *VLA* survey, or due to the slightly elliptical beams noted for some parts of the *NEP* field by Kollgaard et al. (1994), which makes direct comparison difficult, differing *uv* coverage, or due to intrinsic radio source variability. It is also notable that Becker et al. (1995) report that one effect of *CLEAN* bias on *VLA* observations is to reduce the flux. On the basis of this, there appears to be no reason to suspect that the measured *WSRT* integrated fluxes lead to the apparent deficit of sub-mJy sources suggested in Fig. 11.

A search was then made to count how many sources were detected by the Kollgaard et al. (1994) *VLA* survey to a given flux level in comparison to those detected in the *WSRT* survey. Restricting this analysis to the central 0.5 degree diameter area of the *WSRT* mosaic (where the rms peak flux is below ∼30 μJy per beam, the *WSRT* observations recover 307 sources with fluxes above 2 mJy, whereas the *VLA* catalogue contains 53 sources, and an unpublished 610 MHz GMRT image (Sirothia et al., in prep.) recovers about 312 sources (after making approximate flux scaling corrections assuming that the flux to first order follows a $\nu^{0.75}$ relationship). It therefore appears that there are some unexplained discrepancies between the *VLA* survey of Kollgaard and the *WSRT* results, although in term of raw source numbers, the *WSRT* and GMRT data appear to be more consistent, particularly bearing in mind the approximations assumed about spectral indices. Despite these apparent differences, the check carried out and presented here provide no evidence to support the presence of a systematic bias to the *WSRT* differential number counts presented in Figs. 10 and 11, and in the absence of further reasons to be concerned about the *WSRT* counts, it will be assumed that the differences shown in Fig. 11 are most likely due to cosmic variance.

Assuming that faint radio sources have the same correlation length as mJy sources from the *FIRST* and *NVSS* surveys ($r \sim 5$ Mpc; Overzier et al. 2003), and that they sample the redshift interval $z = 1 \pm 0.5$, the rms uncertainty to the differential source counts in a given flux bin from cosmic variance is estimated to be ∼9 per cent (Peacock & Dodds 1994; Eq. (3) of

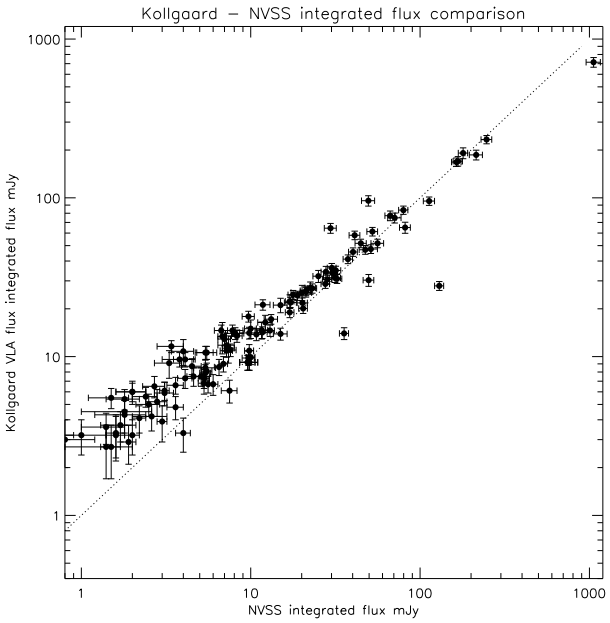

Fig. 7. Cross correlation of the integrated fluxes from the Kollgaard et al. (1994) and the NVSS surveys, with 2σ error bars shown. The fluxes reported by Kollgaard et al. (1994) appear to be systematically higher than the total fluxes reported in the NVSS survey, below ~20 mJy.

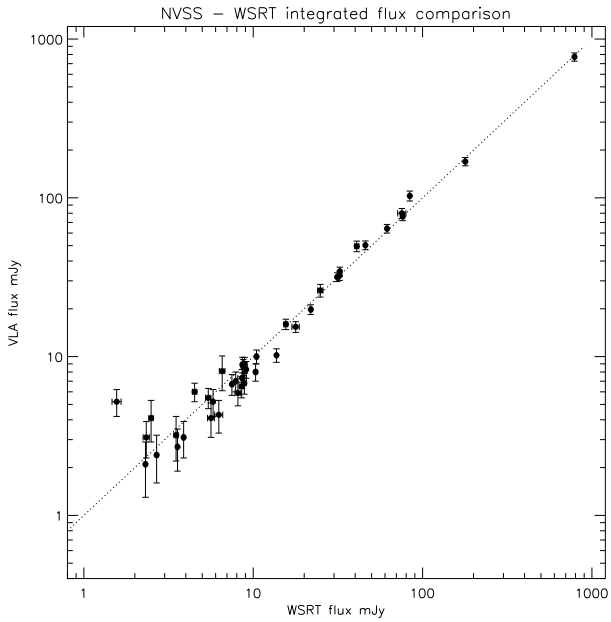

Fig. 8. Comparison of the integrated fluxes of isolated radio sources in common between the *NVSS* survey (45″ beam) and the present *WSRT* data lying within one *WSRT* pixel (4″) of each other. The error bars show the $\pm 2\sigma$ uncertainties. Despite the large difference in the beam sizes, the data show good correlation with each other given the errors for fluxes. In the *WSRT* Deep Boötes field, de Vries et al. (2002) have made a detailed comparison of *NVSS* and *WSRT* fluxes, finding their *WSRT* data systematically lower at fainter flux levels, presumably due to a combination of Malmquist and clean biases close to the *NVSS* limit. It is notable that several of the data points in the present survey also show evidence for this trend. A similar effect has also been reported by comparing *ATCA* and *NVSS* observations by Prandoni et al. (2000b).

Somerville et al. 2004; Simpson et al. 2006), which is comparable with the error spread seen at the lower flux levels.

5.11. Summary of flux density corrections for systematic effects

As discussed in the previous subsections, various systematic effects have been taken into account to estimate the *WSRT* flux densities, including the clean bias and the bandwidth smearing effects. The corrected flux densities reported in Table 1, ($S_{\rm corr}$) have been corrected for the various effects described as follows (following Prandoni et al. 2000b):

$$S_{\rm corr} = \frac{S_{\rm meas}}{k\left[a\log\left(\frac{S_{\rm meas}}{\sigma}\right)+b\right]} \quad (5)$$

where $S_{\rm meas}$ is the flux actually measured in the *WSRT* images (reported in the source catalogue in this paper). The parameter k represents the smearing correction. This has a value of 1 (i.e. no correction) when the equation is applied to integrated flux densities and ≤1 when dealing with peak flux densities. From Fig. 5 we estimate $k = 0.92$ (i.e. an 8% smearing effect which redistributes flux to reduce the *peak* fluxes).

The clean bias correction is taken into account by the term in the square brackets. As discussed by Prandoni et al. (2000b) the importance of the clean bias effect varies across mosaiced images depending on the average number of clean components. For the present data the average number of clean components was 2121, and on the basis of the simulations reported in Sect. 5.3 we adopt $(a, b) = (0.07, 0.82)$. Applying Eq. (5) correctly leads to a good correlation between the *WSRT* and *VLA* fluxes shown in Fig. 8 (where the *WSRT* fluxes were corrected using these parameters).

6. Comparison with other observations

Cross identification with optical data obtained from deep 3.6 m *CFHT* MEGACAM imaging and IR images from the AKARI survey will be included in the next of this series of papers on the NEP Deep Field. An indicative overlay between the radio and r'-band images for the spiral galaxy CGCG 322-021 is shown in Fig. 9. Under seeing conditions of 0.87″ the limiting magnitude in this filter was ~23.5. Further details of the data collection and reduction has been given by Hwang et al. (2007).

7. Differential counts

In Fig. 10 the differential radio source counts are shown from the *NEP* field, normalised to a static Euclidean Universe ($dN/dS\ S^{2.5}$ (sr^{-1} $mJy^{1.5}$)). These source counts are broadly consistent with previous results at 1.4 GHz (e.g. the compilation of Windhorst et al. 1993; the PHOENIX Deep Survey, Hopkins et al. 2003; and the shallow *NEP* survey of Kollgaard et al. 1994).

The data from Fig. 10 are given in Table 1, where the flux bins and mean flux for each of the bin centres are listed in Cols. (1 and 2), the number of sources corrected for clean and resolution bias a discussed in Appendix A are shown in Col. (3), and the number of sources corrected for the area coverage and double sources in Col. 4 (note that because of these correction factors, N_c may be less than N_0), and in Col. (5) we show the differential source counts and the error. The relationship for calculating the numbers in Col. 5 is the same as that presented by Kollgaard et al. (1994).

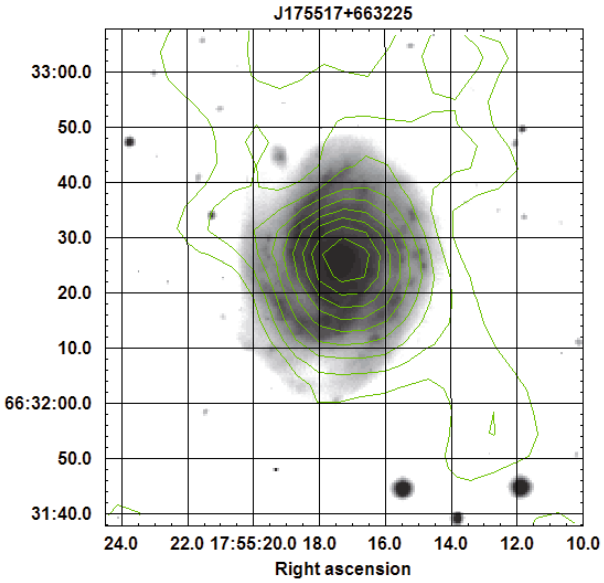

Fig. 9. Overlay between the *WSRT* radio contours and the CFHT *R*-band image for NEP175517+663225 which is coincident with the 15th magnitude spiral galaxy CGCG 322-021 (from the NED Extragalactic database) at redshift $z = 0.0267$. The *WSRT* contours increase linearly to a peak flux of 0.5 mJy beam^{-1}.

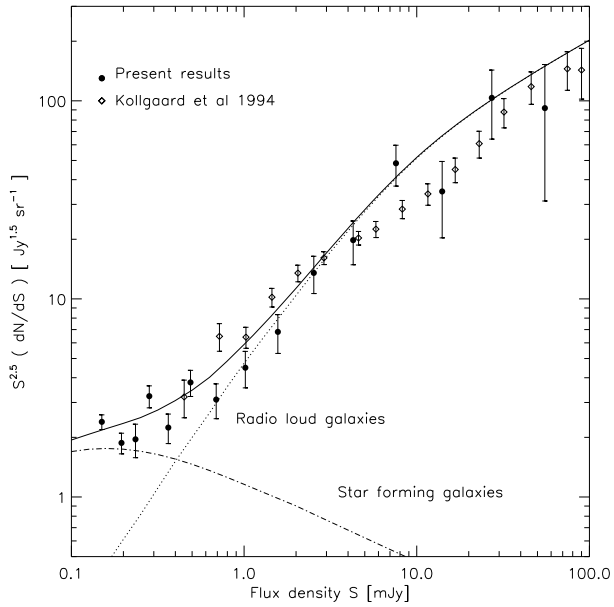

Fig. 10. Differential counts determined from the AKARI *NEP* 20 cm deep field. The *WSRT* data points are shown as filled circles, and the diamonds are show the results from the shallow *VLA* survey by Kollgaard et al. (1994). The data from the two surveys are in reasonable accord, although there are some small differences in the flux scales which are believed to be due to two reasons: **a)** this the same range of flux values where some small differences in the *VLA–WSRT* calibration noted in Fig. 8, **b)** this is the region where the correction for double sources most affects the source counts, and it is not clear whether such a correction was made in the *VLA* analysis. The *VLA* data have smaller error bars at the higher flux values because of the lower number of bright sources in the smaller area of the present survey. The model fit to the source counts is shown as the solid line with the composite radio loud and star-forming galaxy populations plotted as dotted and dash-dot lines respectively.

To model the observed source counts a two component model was used that was made of a classical bright radio loud population and a fainter star-forming population. It is well established that classical bright radio galaxies require strong evolution in order to fit the observed source counts at radio wavelengths (Longair 1966; Rowan-Robinson 1970). The source counts above 10 mJy are dominated by giant radio galaxies and QSOs (powered by accretion onto black holes, commonly joined together in the literature under the generic term AGN). Radio loud sources dominate the source counts down to levels of ∼1 mJy, however, at the sub-mJy level the normalised source counts flatten as a new population of faint radio sources emerge (Windhorst et al. 1985). The dominance of starburst galaxies in the sub-mJy population is already well established (Gruppioni et al. 2008), where the number of blue galaxies with star-forming spectral signatures is seen to increase strongly. Rowan-Robinson et al. (1993), Hopkins et al. (1998), and others have concluded that the source counts at these faintest levels require two populations, AGNs and starburst galaxies. This latter population can best be modelled as a dusty star-forming population, under the assumption that they are the higher redshift analogues of the IRAS star-forming population (Rowan-Robinson et al. 1993; Pearson & Rowan-Robinson 1996). In this scenario, the radio emission originates from the non-thermal synchrotron emission from relativistic electrons accelerated by supernovae remnants in the host galaxies.

To represent the radio loud population the luminosity function of Dunlop & Peacock (1990) was used to model the local space density with an assumption that the population evolves in luminosity with increasing redshift. The assumed luminosity evolution then follows a power law with redshift of $(1 + z)^{3.1}$, broadly consistent with both optically and X-ray selected quasars (Boyle et al. 1987). The spectrum of the radio loud quasar population was modelled from Elvis et al. (1994), assuming a steep radio spectrum source of ($S_\nu \propto \nu^{-\alpha}$, $\alpha = 1$).

Table 1. 20 cm differential source counts for the *WSRT-AKARI-NEP* survey.

Flux bin mJy (1)	Mean flux mJy (2)	N_0 (3)	N_c (4)	dN/dS sr^{-1} Jy$^{1.5}$ (5)
0.130–0.170	0.150	31	138.3	2.39 ± 0.20
0.170–0.220	0.195	31	70.1	1.87 ± 0.22
0.220–0.250	0.235	14	27.02	1.95 ± 0.38
0.250–0.315	0.283	44	61.87	3.23 ± 0.41
0.315–0.413	0.364	33	34.60	2.24 ± 0.38
0.413–0.566	0.489	48	43.95	3.78 ± 0.57
0.566–0.813	0.689	41	24.98	3.10 ± 0.62
0.813–1.221	1.017	40	22.89	4.49 ± 0.94
1.221–1.917	1.569	37	20.31	6.82 ± 1.51
1.917–3.151	2.534	38	21.90	13.53 ± 2.89
3.151–5.416	4.283	29	16.10	19.80 ± 4.93
5.416–9.742	7.597	34	18.38	48.39 ± 11.29
9.742–18.33	14.04	14	5.74	34.87 ± 14.55
18.33–36.08	27.21	10	6.88	103.53 ± 39.47
36.08–74.32	55.20	5	2.29	91.86 ± 60.66

To model the faint sub-mJy population the *IRAS* 60 μm luminosity function of Saunders et al. (2000) was used as a starting point, with the parameters for the star-forming population, segregated by warmer 100 μm/60 μm *IRAS* colour, given in Pearson (2005, in prep). To convert the infrared luminosity

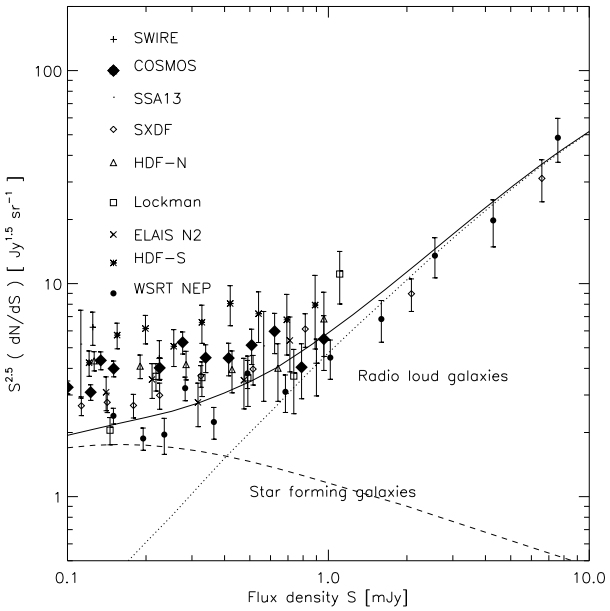

Fig. 11. A compilation of the differential source counts of a number of deep 20 cm radio surveys taken from: SWIRE Owen & Morrison (2008); COSMOS Bondi et al. (2008); SSA13 Fomalont et al. (2006); SXDF Simpson et al. (2006); HDF-N, LOCKMAN and ELAIS N2 Biggs & Ivison (2006), HDF-S Huynh et al. (2005). The solid curve is the best fit to the present data taken as described in Fig. 10. There are however differences in the instrumental and systematic corrections that have been made for the different survey results shown here (see detailed discussion by Prandoni et al. 2000b), that make quantitative comparison at the faintest flux levels somewhat uncertain.

function to radio wavelengths, the well known correlation between the 60 μm far-IR and radio flux emission of $S_{60\,\mu\mathrm{m}} = 90S(1.4\ \mathrm{GHz})$ (Helou et al. 1985; Yun et al. 2001; Appleton et al. 2004; White et al. 2009) was assumed. To model the star-forming population the spectral template of the archetypical starburst galaxy of M 82 from the models of Efstathiou et al. (2000) was adopted. The radio and far-infrared fluxes are correlated due to the presence of hot OB stars in giant molecular clouds that heat the surrounding dust producing the infrared emission. These stars subsequently end their lives as supernovae with the radio emission powered by the synchrotron emission from their remnants. The radio spectrum is characterised by a power law of ($S_\nu \propto \nu^{-\alpha}$, $\alpha = 0.8$).

It was assumed that the star-forming population evolves in luminosity as a power law $\propto(1+z)^{3.0}$. This infrared representation of the star-forming population was preferred over using the radio luminosity function directly, since it creates a phenomenological link between the radio emission and the infrared which is responsible for the bulk of the emission in the star-forming population. Note that Huynh et al. (2005) used the radio luminosity function of Condon et al. (2002) and derived a best fitting evolution parameterisation $\propto(1+z)^{2.7}$, slightly lower than the work presented here although the values are broadly consistent and differences can be due to the assumed SED and luminosity function. Hopkins (2004) and Hopkins et al. (1998) used radio and infrared luminosity functions respectively obtaining evolution in the sub-mJy population $\propto(1+z)^{2.7}$ and $\propto(1+z)^{3.3}$. It does however appear that the counts measured in this study lie at the lower end of the emerging picture on excess sub-mJy radio counts, as shown in Fig. 11.

8. Conclusions

A deep radio survey has been made of an ~1.7 square degree area around the North Ecliptic Pole field using the *WSRT* at 20 cm wavelength. The maximum sensitivity of the survey was 21 μJy beam^{-1}, with a synthesised beam of $17.0 \times 15.5''$. The analysis methodology was carefully chosen to mitigate the various effects that can affect the efficacy of radio synthesis array observations, resulting in a final catalogue of 462 radio emitting sources, with the faintest integrated fluxes at about the 100 μJy level. The differential source counts calculated from the *WSRT* data show a pronounced excess for sources fainter than ~1 mJy, consistent with a population of faint star forming galaxies. Comparison between the Kollgaard et al. (1994) survey and the NVSS catalogue shows a systematic difference in this flux range, suggesting that one or the other may suffer from a slight mis-calibration. The present *WSRT* catalogue of radio sources will form the basis for two further papers reporting cross correlation against extant AKARI and deep optical imaging. A further paper reporting the radio spectral indices of the sources utilising *GMRT* data will be reported elsewhere.

Acknowledgements. This work is based on observations with AKARI, a *JAXA* project with the participation of ESA. We thank Andrew Hopkins for helping us to understand the operation of *SFIND*, Niruj Mohan for discussions on source detection algorithms, and Sandeep Sirothia for discussions about the GMRT 610 MHz NEP survey. We also express our thanks to The Netherlands Institute for Radio Astronomy, *ASTRON*, for the substantial allocation of observing time; the staff of the Westerbork Observatory for technical support; and the UK Science and Technology Facilities Council, *STFC* and its forerunner, *PPARC*, for manpower and travel support. The UK-Japan AKARI Consortium has also received funding awards from the Sasakawa Foundation, The British Council, and the DAIWA Foundation, which facilitated travel and exchange activities, and for which we are very grateful. T.G. acknowledges financial support from the Japan Society for the Promotion of Science (JSPS) through JSPS Research Fellowships for Young Scientists. M.I. was supported by the Korea Science and Engineering Foundation (KOSEF) grant No. 2009-0063616, funded by the Korea government (MEST). HML was supported by National Research Foundation through grant No. 2006-341-C00018.

References

Affer, L., Micela, G., & Morel, T. 2008, A&A, 483, 801
Appleton, P. N., Fadda, D. T., Marleau, F. R., et al. 2004, ApJS, 154, 147
Aussel, H., Coia, D., Mazzei, P., et al. 2000, A&AS, 141, 257
Becker, R. H., White, R. L., & Helfand, D. J. 1995, ApJ, 450, 559
Bennett, C. L., Banday, A. J., Gorski, K. M., et al. 1996, ApJ, 464, 1
Biggs, A. D., & Ivison, R. J. 2006, MNRAS, 371, 963
Bondi, M., Ciliegi, P., Zamorani, G., et al. 2003, A&AS, 403, 857
Bondi, M., Ciliegi, P., Schinnerer, E., et al. 2008, ApJ, 681, 1129
Boyle, B. J., Fong, R., Shanks, T., et al. 1987, MNRAS, 227, 717
Branchesi, M., Gioia, I. M., Fanti, C., et al. 2006, A&A, 446, 97
Bridle, A. H., & Schwab, F. R. 1989, in Synthesis Imaging in Radio Astronomy, ed. R. A. Perley, F. R Schwab, & A. H. Bridle, ASP Conf. Ser., 6, 247
Brinkmann, W., Chester, M., Kollgaard, R., et al. 1999, A&AS, 134, 221; and VizieR On-line Data Catalog: J/A+AS/134/221
Condon, J. J., & Broderick, J. J. 1985, AJ, 90, 2540
Condon, J. J., & Broderick, J. J. 1986, AJ, 91, 1051
Condon, J. J., Cotton, W. D., Greisen, E. W., et al. 1998, AJ, 115, 1693
Condon, J. J., Cotton, W. D., & Broderick, J. J. 2002, AJ, 124, 675
Coppin, K., Chapin, E. L., Mortier, A. M. J., et al. 2006, MNRAS, 372, 1621
Cotton, W. H. 1989, in Synthesis Imaging in Radio Astronomy, ed. R. A. Perley, F. R. Schwab, & A. H. Bridle, ASP Conf. Ser., 6, 233
de Vries, W. H., Morganti, R., Röttgering, H. J. A., et al. 2002, AJ, 1231, 1784
Dunlop, J. S., & Peacock, J. A. 1990, MNRAS, 247, 19
Efstathiou, A., Rowan-Robinson, M., & Siebenmorgen, R. 2000, MNRAS, 313, 734
Elvis, M., Lockman, F. J., & Fassnacht, C. 1994, ApJS, 95, 413
Fomalont, E. B., Kellermann, K. I., Cowie, L. L., et al. 2006, ApJS, 167, 103
Gaidos, E. J., Magnier, E. A., Schechter, P. L., et al. 1993, PASP, 105, 1294
Garn, T., Green, D. A., Riley, J. M., & Alexander, P. 2008, MNRAS, 383, 75
Garrett, M. A., de Bruyn, A. G., Giroletti, M., Baan, W. A., & Schilizzi, R. T. 2000, A&A, 361, 41

Gioia, I. M., Henry, J. P., Mullis, C. R., et al. 2003, ApJS, 149, 29
Gioia, I. M., Wolter, A., Mullis, C. R., et al. 2004, A&A, 428, 867
Goto, T., Hanami, H., Im, M., et al. 2008, PASJ, 60, 531
Gruppioni, C., Pozzi, F., Polletta, M., et al. 2008, MNRAS, 684, 136
Hacking, P., Condon, J. J., & Houck, J. R. 1987, ApJ, 316, L15
Helou, G., Soifer, T. T., & Rowan-Robinson, M. 1985, ApJ, 298, 7
Henry, J. P., Gioia, I. M., Mullis, C. R., et al. 2001, ApJ, 553, 109
Henry, J. P., Mullis, C. R., Voges, W., et al. 2006, ApJS, 162, 304
Hopkins, A. M. 2004, ApJ, 615, 209
Hopkins, A. M., Mobasher, B., Cram, L., et al. 1998, MNRAS, 296, 839
Hopkins, A., Afonso, J., Cram, L., et al. 1999, ApJ, 519, L59
Hopkins, A. M., Miller, C. J., Connolly, A. J., et al. 2002, AJ, 123, 1086
Hopkins, A. M., Afonso, J., Chan, B., et al. 2003, AJ, 125, 465
Huynh, M. T., Jackson, C. A., Norris, R. P., et al. 2005, AJ, 130, 1388
Hwang, N., Lee, H.-M., Im, M., et al. 2007, ApJS, 172, 583
Kaper, H. G., Smiths, D. W., Schwartz, U., et al. 1966, BAN, 18, 465
Kollgaard, R. I., Brinkmann, W., Chester, M. M., et al. 1994, ApJS, 93, 145
Kümmel, M. W., & Wagner, S. J. 2000, A&A, 353, 867
Kümmel, M. W., & Wagner, S. J. 2001, A&A, 370, 384
Lee, H. M., Kim, S. J., Im, M., et al. 2009, PASJ, 61, 375
Loiseau, N., Reich, W., Wielebinski, R., et al. 1988, A&AS, 75, 67
Longair, M. S. 1966, MNRAS, 133, 421
Magliocchetti, M., Maddox, S. J., Lahav, O., et al. 1998, MNRAS, 300, 257
Matsuhara, H., Wada, T., Matsuura, S., et al. 2006, PASJ, 58, 673
Micela, G., Affer, L., Favata, F., et al. 2007, A&A, 461, 977
Morganti, R., Garrett, M. A., Chapman, S., et al. 2004, A&A, 424, 371
Moss, D., Seymour, N., McHardy, I., et al. 2007, MNRAS, 378, 995
Mullis, C. R., Henry, J. P., Gioia, I. M., et al. 2001, ApJ, 553, 115
Mullis, C. R., McNamara, B. R., Quintana, H., et al. 2003, ApJ, 594, 154
Owen, F. R., & Morrison, G. E. 2008, AJ, 136, 1889
Oosterbaan, C. E. 1978, A&A, 69, 235
Overzier, R. A., Rottgering, H. J. A., Rengelink, R. B., et al. 2003, A&A, 405, 53
Pearson, C. P. 2005, MNRAS, 358, 1417
Pearson, C. P., & Rowan-Robinson, M. 1996, MNRAS, 283, 174
Peacock, J. A., & Dodds, S. J. 1994, MNRAS, 267, 1020
Prandoni, I., Gregorini, L., Parma, P., et al. 2000a, A&AS, 146, 31
Prandoni, I., Gregorini, L., Parma, P., et al. 2000b, A&AS, 146, 41
Prandoni, I., Gregorini, L., Parma, P., et al. 2001, A&A, 365, 392
Prandoni, I., Parma, P., Wieringa, M. H., et al. 2006, A&A, 457, 517
Pretorius, M. L., Knigge, C., & O'Donoghue, D. 2007, MNRAS, 382, 1279
Rengelink, R. B., Tang, Y., de Bruyn, A. G., et al. 1997, A&AS, 124, 259
Rowan-Robinson, M. 1970, MNRAS, 149, 365
Rowan-Robinson, M., Benn, C. R., Lawrence, A., et al. 1993, MNRAS, 263, 192
Sault, R. J., Teuben, P. J., & Wright, M. C. H. 1995, Astronomical Data Analysis Software and Systems IV, ed. R. Shaw, H. E. Payne, & J. J. E. Hayes, ASP Conf. Ser., 77, 433
Saunders, W., Sutherland, W. J., Maddox, S. J., et al. 2000, MNRAS, 317, 55
Sedgwick, C., Serjeant, S., Sirothia, S., et al. 2009, in ASP Conf. Ser., ed. T. Onaka, G. J. White, T. Nakagawa, & I. Yamamura, 418, 519
Simpson, C., Martinez-Sansigre, A., Rawlings, S., et al. 2006, MNRAS, 372, 741
Somerville, R. S., Lee, K., Ferguson, H. C., et al. 2004, ApJ, 600, L171
Stickel, M., Bogun, S., Lemke, D., et al. 1998, A&A, 336, 116
Voges, W., Henry, J. P., Briel, U. G., et al. 2001, ApJ, 553, 119
Wada, T., Matsuhara, H., Oyabu, S., et al. 2008, PASJ, 60, 517
White, R. L., Becker, R. H., Helfand, D. J., et al. 1997, ApJ, 475, 479
Windhorst, R. A., Miley G. K., Oweb, F. N., et al. 1985, ApJ, 289, 494
Windhorst, R. A., Fomalont, E. B., Partridge, R. B., et al. 1993, ApJ, 405, 498
Yun, M. S., Reddy, N. A., & Condon, J. J. 2001, ApJ, 554, 803
Zickgraf, F., Thiering, I., Krautter, J., et al. 1997, A&AS, 123, 103

Table 1. The source catalogue.

Running number	Source name	RA	Dec	δRA	δDec	$S_{\rm peak}$	$S_{\rm peak}$ error	$S_{\rm total}$	$S_{\rm total}$ error	$\theta_{\rm maj}$	$\theta_{\rm min}$	PA
		hh:mm:ss.s	dd:mm:ss.s	$''$	$''$	mJy beam^{-1}	mJy beam^{-1}	mJy	mJy	$''$	$''$	$^\circ$
(1)	(2)	(3)	(4)	(5)	(6)	(7)	(8)	(9)	(10)	(11)	(12)	(13)
1	NEP175121+663645	17:51:21.7	+66:36:45.1	1.39	0.22	1.219	0.270	1.932	0.295	28.0		–81.6
2	NEP175140+665038	17:51:41.0	+66:50:38.1	0.01	0.01	2.464	0.364	1.461	0.367			
3	NEP175147+663124	17:51:47.8	+66:31:24.1	0.05	0.04	1.138	0.177	0.829	0.182			
4	NEP175214+665054	17:52:14.7	+66:50:54.2	0.05	0.11	2.615	0.257	5.297	0.288	24.2	13.0	–0.7
5	NEP175231+662738	17:52:31.9	+66:27:38.3	0.38	0.28	0.633	0.148	1.181	0.158	20.6	14.8	–54.6
6	NEP175248+662713	17:52:48.6	+66:27:13.9	0.01	0.01	0.886	0.102	0.885	0.103			
7	NEP175254+663144	17:52:54.5	+66:31:44.1	0.14	0.08	2.774	0.131	7.340	0.184	29.7	17.4	–86.5
8	NEP175256+663148	17:52:56.4	+66:31:48.4	0.74	0.10	2.078	0.131	7.709	0.204	59.6	9.7	85.5
9	NEP175305+663929	17:53:06.0	+66:39:29.8	0.02	0.01	1.708	0.121	2.216	0.131			
10	NEP175307+663213	17:53:07.6	+66:32:13.2	0.02	0.02	3.735	0.131	8.035	0.202	21.1	17.4	8.4
11	NEP175313+661949	17:53:13.9	+66:19:49.7	0.00	0.00	6.197	0.148	8.574	0.186			
12	NEP175321+661249	17:53:21.5	+66:12:49.1	0.04	0.03	1.403	0.149	1.673	0.153			
13	NEP175330+662831	17:53:30.0	+66:28:31.5	0.00	0.00	1.056	0.086	1.248	0.090			
14	NEP175331+662726	17:53:31.3	+66:27:26.6	0.00	0.00	26.929	0.086	32.232	0.147			
15	NEP175334+665105	17:53:34.8	+66:51:05.2	0.01	0.00	1.503	0.148	2.112	0.149			
16	NEP175335+663547	17:53:35.1	+66:35:47.9	0.00	0.00	152.400	0.224	180.740	0.585			
17	NEP175336+663438	17:53:36.0	+66:34:38.8	0.00	0.00	41.663	0.147	61.508	0.322			
18	NEP175338+663135	17:53:38.4	+66:31:35.4	0.02	0.03	5.419	0.090	8.668	0.267			
19	NEP175338+665105	17:53:38.8	+66:51:05.2	0.00	0.00	1.503	0.148	2.321	0.380			
20	NEP175339+663319	17:53:39.3	+66:33:19.3	0.01	0.01	1.197	0.147	1.120	0.148			
21	NEP175348+663922	17:53:48.3	+66:39:22.7	0.00	0.00	0.736	0.081	0.715	0.084			
22	NEP175357+670348	17:53:57.8	+67:03:48.4	0.05	0.03	3.387	0.327	6.131	0.350	25.2	9.5	–58.6
23	NEP175358+664929	17:53:58.6	+66:49:29.6	0.07	0.05	1.111	0.101	1.738	0.114	18.6	10.7	–64.5
24	NEP175410+664620	17:54:10.2	+66:46:20.3	0.03	0.06	0.652	0.084	0.987	0.087	24.2		–5.9
25	NEP175412+663401	17:54:12.8	+66:34:02.0	0.03	0.02	0.410	0.063	0.476	0.065			
26	NEP175419+660245	17:54:19.9	+66:02:45.7	0.11	0.14	1.839	0.360	5.392	0.386	28.6	22.3	–13.0
27	NEP175420+663059	17:54:20.4	+66:30:59.1	0.00	0.00	2.681	0.048	2.822	0.055			
28	NEP175437+662248	17:54:37.3	+66:22:48.6	0.01	0.01	0.722	0.072	0.826	0.073			
29	NEP175438+662319	17:54:38.8	+66:23:19.0	0.01	0.01	0.708	0.072	0.740	0.074			
30	NEP175445+664823	17:54:45.5	+66:48:24.0	0.03	0.03	0.626	0.064	0.737	0.067			
31	NEP175445+661208	17:54:46.0	+66:12:08.7	0.01	0.01	14.286	0.091	25.459	0.455	17.6	13.6	81.2
32	NEP175454+663417	17:54:54.0	+66:34:17.6	0.06	0.04	0.227	0.038	0.171	0.039			
33	NEP175455+665658	17:54:55.4	+66:56:58.3	0.00	0.00	3.637	0.124	4.334	0.141			
34	NEP175458+661723	17:54:58.9	+66:17:23.7	0.01	0.01	1.453	0.070	1.546	0.079			
35	NEP175459+661139	17:54:59.3	+66:11:39.9	0.02	0.03	3.273	0.085	4.427	0.155			
36	NEP170550+663153	17:055:0.0	+66:31:53.2	0.01	0.01	0.390	0.051	0.421	0.051			
37	NEP175504+663952	17:55:04.8	+66:39:52.7	0.00	0.00	8.001	0.055	8.472	0.064			
38	NEP175506+661737	17:55:06.6	+66:17:37.7	0.00	0.00	6.142	0.070	6.925	0.092			
39	NEP175509+663400	17:55:09.4	+66:34:00.0	0.00	0.00	2.115	0.038	2.455	0.045			
40	NEP175512+663040	17:55:12.6	+66:30:40.1	0.04	0.06	1.657	0.051	3.415	0.083	24.3	12.7	–28.5

Table 1. continued.

Running number	Source name	RA	Dec	δRA	δDec	$S_{\rm peak}$	$S_{\rm peak}$ error	$S_{\rm total}$	$S_{\rm total}$ error	$\theta_{\rm maj}$	$\theta_{\rm min}$	PA
		hh:mm:ss.s	dd:mm:ss.s	$''$	$''$	mJy beam^{-1}	mJy beam^{-1}	mJy	mJy	$''$	$''$	$^\circ$
(1)	(2)	(3)	(4)	(5)	(6)	(7)	(8)	(9)	(10)	(11)	(12)	(13)
41	NEP175513+663111	17:55:13.5	+66:31:11.8	0.04	0.03	3.626	0.045	7.360	0.195	21.3	14.2	56.3
42	NEP175515+655429	17:55:15.2	+65:54:29.7	0.04	0.05	2.220	0.348	1.766	0.359			
43	NEP175515+661703	17:55:15.8	+66:17:03.7	0.01	0.01	1.361	0.070	1.606	0.077			
44	NEP175516+662425	17:55:16.9	+66:24:25.6	0.00	0.00	1.263	0.037	1.341	0.042			
45	NEP175517+662812	17:55:17.0	+66:28:13.0	0.01	0.01	0.258	0.041	0.179	0.041			
46	NEP175517+663225	17:55:17.1	+66:32:25.6	0.04	0.05	0.517	0.045	1.158	0.051	23.3	17.5	3.1
47	NEP175517+663919	17:55:17.4	+66:39:19.2	0.02	0.03	0.527	0.036	0.604	0.040			
48	NEP175517+661658	17:55:17.4	+66:16:58.8	0.95	0.53	0.819	0.055	1.991	0.085	27.7	15.9	–63.5
49	NEP175520+662428	17:55:20.9	+66:24:28.2	0.00	0.00	0.410	0.037	0.631	0.046	19.4	8.8	–64.2
50	NEP175521+663526	17:55:21.7	+66:35:26.2	0.02	0.01	0.397	0.043	0.408	0.044			
51	NEP175521+661338	17:55:21.9	+66:13:38.4	0.05	0.02	38.490	0.135	79.820	2.134	22.6	12.8	–89.9
52	NEP175523+662404	17:55:23.8	+66:24:04.7	0.01	0.02	0.897	0.037	0.879	0.045			
53	NEP175526+665356	17:55:26.8	+66:53:56.0	0.00	0.00	6.096	0.084	7.244	0.100			
54	NEP175527+662351	17:55:27.0	+66:23:51.2	0.10	0.09	0.678	0.037	0.968	0.057			
55	NEP175529+662416	17:55:29.6	+66:24:16.0	0.11	0.11	0.199	0.037	0.290	0.039	17.6	9.7	60.0
56	NEP175533+663116	17:55:33.2	+66:31:16.8	0.00	0.00	0.470	0.045	0.409	0.045			
57	NEP175535+662744	17:55:35.8	+66:27:44.4	0.03	0.05	0.237	0.041	0.295	0.042			
58	NEP175537+664550	17:55:37.7	+66:45:50.1	0.24	0.06	0.239	0.046	0.378	0.049	25.1	5.0	88.5
59	NEP175545+664037	17:55:45.3	+66:40:37.4	0.33	0.24	0.177	0.039	0.255	0.041	20.9	4.8	60.5
60	NEP175546+663839	17:55:46.2	+66:38:39.5	0.07	0.11	0.247	0.039	0.320	0.041	18.3		–30.7
61	NEP175548+670656	17:55:48.1	+67:06:56.8	0.63	0.51	0.948	0.198	3.173	0.235	29.7	25.8	–62.1
62	NEP175550+671240	17:55:50.4	+67:12:40.9	1.61	0.45	3.369	0.383	1.212	0.383			
63	NEP175552+662635	17:55:52.2	+66:26:35.8	0.11	0.18	0.255	0.041	0.513	0.046	26.2	11.1	23.0
64	NEP175555+663629	17:55:55.6	+66:36:29.2	0.15	0.10	0.223	0.035	0.167	0.038			
65	NEP175601+660829	17:56:01.1	+66:08:29.8	0.02	0.02	1.803	0.093	3.058	0.112	19.7	11.3	23.2
66	NEP175601+663500	17:56:01.9	+66:35:00.0	0.14	0.14	0.330	0.035	0.427	0.041			
67	NEP175602+661824	17:56:02.1	+66:18:24.7	0.00	0.00	1.421	0.044	1.467	0.048			
68	NEP175604+660805	17:56:04.7	+66:08:05.9	0.03	0.04	0.925	0.093	1.266	0.099			
69	NEP175608+664119	17:56:08.2	+66:41:19.6	0.00	0.01	0.361	0.039	0.369	0.039			
70	NEP175608+664424	17:56:08.7	+66:44:24.2	0.01	0.01	0.712	0.045	0.725	0.047			
71	NEP175609+663304	17:56:09.6	+66:33:04.5	0.00	0.00	0.555	0.035	0.542	0.036			
72	NEP175611+663542	17:56:11.5	+66:35:42.0	0.04	0.08	0.202	0.031	0.177	0.033			
73	NEP175612+661731	17:56:12.7	+66:17:31.9	0.05	0.04	0.234	0.043	0.276	0.044			
74	NEP175615+664653	17:56:15.8	+66:46:53.8	0.03	0.04	0.367	0.036	0.363	0.038			
75	NEP175620+664340	17:56:20.8	+66:43:40.8	0.14	0.06	1.116	0.039	2.864	0.091	32.6	13.3	67.1
76	NEP175621+661649	17:56:21.7	+66:16:50.0	0.01	0.01	0.548	0.040	0.512	0.041			
77	NEP175625+663243	17:56:25.2	+66:32:43.4	0.01	0.01	1.323	0.034	1.620	0.047			
78	NEP175628+663820	17:56:29.0	+66:38:20.6	0.04	0.03	0.338	0.031	0.364	0.033			
79	NEP175631+662509	17:56:31.8	+66:25:09.6	0.06	0.11	0.163	0.029	0.175	0.030			
80	NEP175634+665317	17:56:34.3	+66:53:17.5	0.02	0.03	0.318	0.060	0.305	0.061			

Table 1. continued.

Running number	Source name	RA	Dec	δRA	δDec	$S_{\rm peak}$	$S_{\rm peak}$ error	$S_{\rm total}$	$S_{\rm total}$ error	$\theta_{\rm maj}$	$\theta_{\rm min}$	PA
		hh:mm:ss.s	dd:mm:ss.s	$''$	$''$	mJy beam^{-1}	mJy beam^{-1}	mJy	mJy	$''$	$''$	$^\circ$
(1)	(2)	(3)	(4)	(5)	(6)	(7)	(8)	(9)	(10)	(11)	(12)	(13)
81	NEP175636+663911	17:56:36.5	+66:39:11.8	0.18	0.25	0.152	0.036	0.318	0.038	25.2	13.9	31.4
82	NEP175636+663117	17:56:36.5	+66:31:17.4	2.16	0.98	0.109	0.027	0.344	0.031	30.5	22.9	70.5
83	NEP175636+671349	17:56:36.7	+67:13:49.6	0.04	0.04	4.100	0.417	6.276	0.442	17.9	10.4	–36.2
84	NEP175637+664025	17:56:37.1	+66:40:25.9	0.04	0.04	0.396	0.036	0.441	0.039			
85	NEP175638+663147	17:56:38.8	+66:31:47.1	0.06	0.03	0.133	0.027	0.119	0.027			
86	NEP175639+664800	17:56:39.9	+66:48:00.8	0.00	0.00	0.672	0.038	0.706	0.039			
87	NEP175640+670444	17:56:40.6	+67:04:44.3	0.00	0.00	8.093	0.100	10.113	0.138			
88	NEP175640+663416	17:56:40.9	+66:34:16.6	0.00	0.00	0.296	0.034	0.250	0.035			
89	NEP175641+661528	17:56:41.4	+66:15:28.1	0.00	0.00	1.681	0.040	1.701	0.044			
90	NEP175642+663333	17:56:42.5	+66:33:33.2	0.00	0.00	40.429	0.042	47.392	0.192			
91	NEP175644+663738	17:56:44.2	+66:37:38.1	0.06	0.03	0.197	0.033	0.164	0.034			
92	NEP175648+662737	17:56:48.2	+66:27:37.9	0.09	0.08	0.687	0.031	0.868	0.061			
93	NEP175651+661308	17:56:51.4	+66:13:08.2	0.03	0.03	0.324	0.057	0.351	0.058			
94	NEP175651+662058	17:56:51.4	+66:20:58.8	0.04	0.04	0.202	0.032	0.147	0.033			
95	NEP175652+661144	17:56:52.6	+66:11:44.5	0.02	0.01	1.348	0.053	2.346	0.066	21.9	10.5	59.5
96	NEP175653+664532	17:56:53.9	+66:45:33.0	0.02	0.02	0.862	0.033	0.949	0.047			
97	NEP175655+662940	17:56:55.9	+66:29:40.1	0.03	0.04	0.176	0.031	0.190	0.032			
98	NEP175657+655745	17:56:57.1	+65:57:45.0	0.04	0.05	0.596	0.113	0.723	0.115			
99	NEP175658+662358	17:56:58.7	+66:23:58.9	0.07	0.08	0.170	0.033	0.189	0.034			
100	NEP175702+661328	17:57:02.3	+66:13:29.0	0.00	0.00	7.180	0.057	7.652	0.067			
101	NEP175702+662404	17:57:02.4	+66:24:04.4	0.02	0.03	0.208	0.033	0.178	0.034			
102	NEP175703+670910	17:57:03.3	+67:09:10.4	0.00	0.00	2.493	0.190	2.746	0.199			
103	NEP175703+663058	17:57:03.5	+66:30:58.0	0.01	0.02	0.191	0.034	0.148	0.034			
104	NEP175703+665418	17:57:03.8	+66:54:18.8	0.00	0.00	27.315	0.069	32.128	0.113			
105	NEP175706+664903	17:57:06.4	+66:49:03.4	0.03	0.05	0.253	0.038	0.217	0.040			
106	NEP175707+664132	17:57:07.7	+66:41:32.7	0.07	0.23	0.230	0.031	0.458	0.036	29.6	5.9	3.8
107	NEP175707+661917	17:57:07.8	+66:19:17.5	0.01	0.02	1.130	0.032	1.523	0.049			
108	NEP175711+662221	17:57:11.7	+66:22:21.1	0.01	0.02	0.359	0.032	0.328	0.033			
109	NEP175714+662139	17:57:14.4	+66:21:39.2	0.00	0.00	0.156	0.027	0.096	0.027			
110	NEP175714+662529	17:57:14.5	+66:25:29.0	0.01	0.01	0.184	0.030	0.129	0.030			
111	NEP175715+665449	17:57:15.4	+66:54:49.6	0.01	0.04	0.629	0.046	0.641	0.051			
112	NEP175715+661605	17:57:15.7	+66:16:05.2	0.27	0.17	0.210	0.037	0.611	0.041	31.0	20.1	–61.6
113	NEP175718+664726	17:57:18.9	+66:47:26.9	0.15	0.26	0.179	0.038	0.244	0.041	18.6	2.2	–9.6
114	NEP175721+662945	17:57:21.2	+66:29:45.8	0.01	0.01	0.467	0.031	0.421	0.032			
115	NEP175722+670332	17:57:22.2	+67:03:32.1	0.02	0.05	0.627	0.092	0.808	0.096	19.7		–13.5
116	NEP175725+661546	17:57:25.7	+66:15:46.0	0.03	0.04	0.295	0.037	0.364	0.038			
117	NEP175727+664557	17:57:27.7	+66:45:57.1	0.01	0.01	0.281	0.035	0.229	0.035			
118	NEP175728+663822	17:57:28.2	+66:38:22.1	0.10	0.06	0.674	0.030	1.077	0.055	18.8	9.8	65.4
119	NEP175729+660947	17:57:29.0	+66:09:47.9	0.09	0.19	0.293	0.051	0.387	0.055	19.9		16.4
120	NEP175729+662417	17:57:29.4	+66:24:17.1	0.03	0.03	0.215	0.030	0.175	0.031			

Table 1. continued.

Running number	Source name	RA	Dec	δRA	δDec	$S_{\rm peak}$	$S_{\rm peak}$ error	$S_{\rm total}$	$S_{\rm total}$ error	$\theta_{\rm maj}$	$\theta_{\rm min}$	PA
		hh:mm:ss.s	dd:mm:ss.s	$''$	$''$	mJy beam^{-1}	mJy beam^{-1}	mJy	mJy	$''$	$''$	$^\circ$
(1)	(2)	(3)	(4)	(5)	(6)	(7)	(8)	(9)	(10)	(11)	(12)	(13)
121	NEP175731+670433	17:57:31.7	+67:04:33.7	0.00	0.00	17.560	0.092	21.016	0.176			
122	NEP175732+663625	17:57:32.3	+66:36:25.8	0.91	0.18	0.129	0.030	0.353	0.033	39.8	12.1	89.3
123	NEP175732+654853	17:57:33.0	+65:48:53.7	0.02	0.32	1.953	0.372	2.477	0.389	19.5		13.7
124	NEP175734+654859	17:57:34.4	+65:48:59.3	1.33	1.90	1.603	0.372	4.732	0.412	30.8	20.6	57.2
125	NEP175735+662206	17:57:35.3	+66:22:06.8	0.01	0.02	0.174	0.027	0.139	0.027			
126	NEP175737+665439	17:57:37.5	+66:54:39.6	0.00	0.00	0.709	0.046	0.733	0.048			
127	NEP175737+664443	17:57:37.8	+66:44:43.3	0.01	0.01	4.166	0.035	5.486	0.130			
128	NEP175740+662830	17:57:40.0	+66:28:30.6	0.01	0.02	0.809	0.031	0.813	0.040			
129	NEP175740+664550	17:57:40.3	+66:45:50.3	0.05	0.22	1.364	0.036	2.976	0.113	31.0	6.1	12.5
130	NEP175743+662644	17:57:43.8	+66:26:44.4	0.02	0.02	0.177	0.027	0.125	0.027			
131	NEP175744+663718	17:57:44.1	+66:37:18.4	0.18	0.15	0.138	0.030	0.309	0.031	28.9	13.4	–43.5
132	NEP175744+664358	17:57:44.4	+66:43:58.3	0.04	0.03	0.197	0.036	0.132	0.037			
133	NEP175744+660932	17:57:44.8	+66:09:32.8	0.00	0.01	1.916	0.054	2.085	0.064			
134	NEP175745+662904	17:57:45.4	+66:29:04.8	0.02	0.04	0.169	0.025	0.126	0.025			
135	NEP175746+665437	17:57:46.5	+66:54:37.2	0.02	0.02	0.275	0.044	0.452	0.045	21.8	9.3	–39.1
136	NEP175746+661022	17:57:47.0	+66:10:22.9	0.04	0.07	0.325	0.054	0.366	0.056			
137	NEP175748+665903	17:57:48.5	+66:59:03.7	0.02	0.08	0.622	0.045	0.932	0.052	25.8		8.8
138	NEP175748+655340	17:57:48.9	+65:53:40.7	0.01	0.02	2.741	0.214	3.354	0.227			
139	NEP175749+663132	17:57:49.7	+66:31:32.8	0.04	0.04	0.158	0.027	0.289	0.028	20.0	14.9	7.0
140	NEP175753+670042	17:57:53.6	+67:00:42.2	0.00	0.00	0.551	0.065	0.449	0.065			
141	NEP175754+664857	17:57:54.9	+66:48:57.1	0.00	0.00	3.588	0.040	3.792	0.050			
142	NEP175755+662857	17:57:55.5	+66:28:57.3	0.02	0.03	0.141	0.025	0.124	0.025			
143	NEP175756+660925	17:57:56.7	+66:09:25.8	0.01	0.01	0.822	0.054	0.835	0.057			
144	NEP175758+662927	17:57:59.0	+66:29:27.4	0.01	0.01	0.206	0.025	0.155	0.025			
145	NEP175803+663547	17:58:03.0	+66:35:47.6	0.09	0.11	0.455	0.030	0.683	0.043	18.3	7.6	32.3
146	NEP175804+661103	17:58:04.5	+66:11:03.9	0.02	0.02	0.281	0.054	0.233	0.054			
147	NEP175805+663620	17:58:05.4	+66:36:20.3	0.50	0.16	0.186	0.030	0.436	0.036	31.0	12.8	–72.8
148	NEP175805+662527	17:58:05.5	+66:25:27.2	0.01	0.01	0.177	0.027	0.123	0.027			
149	NEP175807+663640	17:58:07.9	+66:36:40.4	1.42	0.26	0.149	0.030	0.317	0.034	27.5	13.0	82.6
150	NEP175808+664909	17:58:08.4	+66:49:09.9	0.00	0.00	13.260	0.040	13.573	0.058			
151	NEP175809+661532	17:58:09.4	+66:15:32.1	0.00	0.00	1.050	0.032	1.073	0.037			
152	NEP175809+664134	17:58:09.4	+66:41:34.9	0.00	0.00	7.367	0.036	10.512	0.094	18.1	2.7	–21.9
153	NEP175813+661516	17:58:13.3	+66:15:16.1	0.02	0.01	0.179	0.028	0.142	0.028			
154	NEP175813+661225	17:58:13.8	+66:12:25.6	0.03	0.05	0.242	0.047	0.280	0.048			
155	NEP175814+664425	17:58:14.4	+66:44:25.2	0.00	0.00	3.196	0.031	3.185	0.040			
156	NEP175816+661149	17:58:16.3	+66:11:49.3	0.04	0.02	1.088	0.048	1.963	0.068	20.8	12.6	70.7
157	NEP175816+661006	17:58:16.8	+66:10:06.1	0.00	0.00	0.563	0.048	0.479	0.048			
158	NEP175818+664325	17:58:18.3	+66:43:25.8	0.03	0.02	0.167	0.031	0.144	0.031			
159	NEP175819+661231	17:58:19.7	+66:12:31.1	0.00	0.00	3.046	0.047	3.451	0.051			
160	NEP175820+670207	17:58:20.2	+67:02:07.3	0.07	0.14	0.413	0.080	0.444	0.084			

Table 1. continued.

Running number	Source name	RA	Dec	δRA	δDec	$S_{\rm peak}$	$S_{\rm peak}$ error	$S_{\rm total}$	$S_{\rm total}$ error	$\theta_{\rm maj}$	$\theta_{\rm min}$	PA
		hh:mm:ss.s	dd:mm:ss.s	$''$	$''$	mJy beam^{-1}	mJy beam^{-1}	mJy	mJy	$''$	$''$	$^\circ$
(1)	(2)	(3)	(4)	(5)	(6)	(7)	(8)	(9)	(10)	(11)	(12)	(13)
161	NEP175821+662855	17:58:21.3	+66:28:55.9	0.00	0.00	1.010	0.026	1.087	0.028			
162	NEP175821+661349	17:58:21.6	+66:13:49.5	0.00	0.00	6.011	0.047	6.883	0.079			
163	NEP175823+662121	17:58:23.6	+66:21:21.6	0.01	0.02	0.167	0.029	0.151	0.029			
164	NEP175824+663912	17:58:24.1	+66:39:12.7	0.58	0.40	0.212	0.036	0.293	0.041	23.8		52.9
165	NEP175824+665814	17:58:24.6	+66:58:14.9	0.04	0.07	0.615	0.056	0.604	0.061			
166	NEP175824+664420	17:58:24.8	+66:44:20.3	0.00	0.01	0.385	0.031	0.283	0.032			
167	NEP175826+670148	17:58:26.9	+67:01:48.5	0.01	0.01	6.004	0.059	8.601	0.157			
168	NEP175826+655505	17:58:27.0	+65:55:05.9	0.10	0.07	21.968	3.026	191.847	3.257	52.5	48.2	82.5
169	NEP175827+665112	17:58:27.3	+66:51:12.8	0.03	0.04	0.293	0.042	0.309	0.043			
170	NEP175827+665537	17:58:27.5	+66:55:37.5	0.02	0.03	0.270	0.040	0.237	0.041			
171	NEP175828+665811	17:58:28.7	+66:58:11.6	1.06	0.42	0.210	0.056	0.672	0.062	30.4	24.0	87.0
172	NEP175830+664926	17:58:30.1	+66:49:26.2	0.00	0.01	1.668	0.045	2.864	0.055	24.3	5.8	23.5
173	NEP175830+663932	17:58:31.0	+66:39:32.6	0.25	0.14	0.197	0.036	0.264	0.041			
174	NEP175831+661145	17:58:31.1	+66:11:45.1	0.01	0.03	0.304	0.048	0.245	0.049			
175	NEP175831+662318	17:58:31.9	+66:23:18.4	0.00	0.00	1.237	0.029	1.326	0.030			
176	NEP175832+662722	17:58:32.8	+66:27:23.0	0.25	0.28	0.130	0.026	0.220	0.027	29.2		–48.9
177	NEP175832+655259	17:58:33.0	+65:52:59.6	0.01	0.01	12.632	0.742	76.257	0.829	43.3	37.5	40.4
178	NEP175833+663759	17:58:33.3	+66:37:59.5	0.00	0.00	509.459	1.133	786.233	2.568			
179	NEP175835+662953	17:58:35.3	+66:29:53.2	0.03	0.02	0.140	0.029	0.128	0.029			
180	NEP175835+663843	17:58:36.0	+66:38:43.9	0.51	0.93	0.208	0.036	0.393	0.038	27.6	8.6	–49.4
181	NEP175838+663733	17:58:38.6	+66:37:33.4	****	6.24	0.545	1.133	1.881	1.134	36.8	24.4	–56.5
182	NEP175840+663727	17:58:40.3	+66:37:27.6	4.30	1.09	0.317	0.044	1.045	0.057	33.8	20.9	18.8
183	NEP175840+663920	17:58:40.6	+66:39:20.9	0.16	0.24	0.156	0.033	0.273	0.035	26.6	5.2	–28.5
184	NEP175840+662212	17:58:40.7	+66:22:12.5	0.08	0.08	0.350	0.030	0.514	0.036			
185	NEP175843+663419	17:58:43.6	+66:34:19.8	0.00	0.01	0.189	0.028	0.123	0.028			
186	NEP175846+661341	17:58:46.3	+66:13:41.6	0.00	0.00	0.409	0.035	0.387	0.035			
187	NEP175846+660732	17:58:46.4	+66:07:32.2	0.04	0.03	0.261	0.045	0.210	0.046			
188	NEP175846+664759	17:58:46.6	+66:47:59.7	0.01	0.01	0.262	0.035	0.208	0.035			
189	NEP175847+661418	17:58:47.9	+66:14:18.9	0.01	0.01	0.455	0.035	0.466	0.036			
190	NEP175848+660949	17:58:48.9	+66:09:49.2	0.02	0.04	0.357	0.040	0.390	0.041			
191	NEP175849+660716	17:58:49.7	+66:07:16.2	0.01	0.01	0.634	0.045	0.647	0.047			
192	NEP175850+663736	17:58:50.1	+66:37:36.8	0.10	0.12	0.246	0.044	0.264	0.047			
193	NEP175852+662934	17:58:52.1	+66:29:34.8	0.00	0.00	3.549	0.026	3.517	0.035			
194	NEP175852+662008	17:58:52.6	+66:20:08.7	0.00	0.00	1.665	0.031	1.818	0.043			
195	NEP175853+670636	17:58:53.2	+67:06:36.0	0.01	0.01	5.382	0.105	7.120	0.163			
196	NEP175853+662320	17:58:53.3	+66:23:20.9	0.09	0.05	0.148	0.030	0.174	0.031			
197	NEP175856+661912	17:58:56.6	+66:19:12.8	0.12	0.17	0.156	0.031	0.268	0.033	19.2	13.0	–1.0
198	NEP175857+664932	17:58:57.3	+66:49:32.2	0.00	0.01	1.651	0.035	1.877	0.047			
199	NEP175859+663017	17:58:59.6	+66:30:17.5	0.02	0.02	0.435	0.028	0.419	0.031			
200	NEP175904+661339	17:59:04.9	+66:13:39.5	0.00	0.00	1.745	0.035	1.715	0.041			

Table 1. continued.

Running number	Source name	RA	Dec	δRA	δDec	$S_{\rm peak}$	$S_{\rm peak}$ error	$S_{\rm total}$	$S_{\rm total}$ error	$\theta_{\rm maj}$	$\theta_{\rm min}$	PA
		hh:mm:ss.s	dd:mm:ss.s	$''$	$''$	mJy beam^{-1}	mJy beam^{-1}	mJy	mJy	$''$	$''$	$^\circ$
(1)	(2)	(3)	(4)	(5)	(6)	(7)	(8)	(9)	(10)	(11)	(12)	(13)
201	NEP175905+662144	17:59:05.1	+66:21:45.0	0.01	0.01	0.738	0.030	0.754	0.034			
202	NEP175905+661605	17:59:05.3	+66:16:05.8	0.00	0.01	1.787	0.031	1.870	0.048			
203	NEP175905+664804	17:59:05.8	+66:48:04.8	0.00	0.01	0.342	0.035	0.312	0.035			
204	NEP175905+663229	17:59:05.9	+66:32:29.8	0.00	0.00	0.309	0.028	0.281	0.028			
205	NEP175908+662516	17:59:08.3	+66:25:16.1	0.00	0.00	0.474	0.027	0.450	0.027			
206	NEP175909+663924	17:59:09.8	+66:39:24.5	0.00	0.00	1.038	0.035	0.995	0.036			
207	NEP175910+664002	17:59:10.4	+66:40:02.9	0.01	0.01	0.458	0.035	0.481	0.036			
208	NEP175911+660427	17:59:11.1	+66:04:27.6	0.01	0.01	0.482	0.062	0.517	0.063			
209	NEP175911+665014	17:59:11.1	+66:50:14.3	0.00	0.00	1.021	0.035	0.987	0.038			
210	NEP175911+663004	17:59:11.1	+66:30:04.9	0.01	0.02	0.256	0.029	0.235	0.029			
211	NEP175911+660450	17:59:11.6	+66:04:51.0	0.42	1.24	0.327	0.062	0.555	0.069	23.0	8.0	–30.8
212	NEP175911+663348	17:59:11.9	+66:33:49.0	0.00	0.00	1.091	0.028	0.975	0.032			
213	NEP175915+663302	17:59:15.4	+66:33:02.8	0.01	0.01	0.769	0.028	0.784	0.034			
214	NEP175916+661031	17:59:16.8	+66:10:31.7	0.02	0.02	0.348	0.043	0.344	0.044			
215	NEP175919+660636	17:59:19.7	+66:06:36.3	0.03	0.04	0.464	0.053	0.609	0.055			
216	NEP175921+664235	17:59:21.4	+66:42:35.1	0.01	0.01	0.259	0.032	0.188	0.032			
217	NEP175921+663858	17:59:21.6	+66:38:58.6	0.01	0.01	0.959	0.035	0.931	0.041			
218	NEP175922+665036	17:59:22.4	+66:50:36.3	0.00	0.00	0.956	0.036	1.009	0.039			
219	NEP175923+654958	17:59:23.1	+65:49:58.7	0.03	0.06	3.310	0.278	4.754	0.312	19.5	3.8	5.2
220	NEP175926+661440	17:59:26.0	+66:14:40.4	0.16	0.08	0.151	0.030	0.426	0.031	30.4	20.3	77.1
221	NEP175926+662941	17:59:26.4	+66:29:41.0	0.01	0.04	0.170	0.029	0.168	0.029			
222	NEP175927+664229	17:59:27.6	+66:42:29.9	0.01	0.02	0.275	0.032	0.276	0.033			
223	NEP175929+663227	17:59:29.1	+66:32:27.2	0.01	0.01	0.222	0.029	0.210	0.029			
224	NEP175930+655642	17:59:30.6	+65:56:42.9	0.00	0.01	2.865	0.139	3.325	0.148			
225	NEP175931+662906	17:59:31.8	+66:29:06.9	0.00	0.00	0.269	0.029	0.247	0.029			
226	NEP175933+661226	17:59:33.5	+66:12:26.5	0.43	0.15	0.142	0.030	0.765	0.033	51.1	27.5	89.9
227	NEP175934+662704	17:59:34.4	+66:27:04.5	0.00	0.00	0.430	0.029	0.381	0.030			
228	NEP175934+670214	17:59:34.5	+67:02:14.2	0.00	0.00	2.351	0.074	2.678	0.083			
229	NEP175934+661306	17:59:34.6	+66:13:06.5	0.01	0.01	0.361	0.030	0.342	0.031			
230	NEP175935+662104	17:59:35.5	+66:21:04.3	0.61	1.12	0.117	0.028	0.270	0.030	26.9	15.4	–12.5
231	NEP175936+661604	17:59:36.2	+66:16:04.4	0.00	0.00	20.371	0.132	21.707	0.207			
232	NEP175936+671856	17:59:36.7	+67:18:56.3	0.03	0.14	2.504	0.416	2.346	0.421			
233	NEP175937+661316	17:59:37.8	+66:13:16.8	1.16	2.04	0.123	0.030	0.659	0.034	40.6	34.8	28.0
234	NEP175937+671726	17:59:37.8	+67:17:26.6	0.01	0.01	9.394	0.475	14.724	0.518	20.4	7.6	3.7
235	NEP175938+655841	17:59:38.1	+65:58:41.7	0.00	0.00	1.054	0.094	0.368	0.095			
236	NEP175940+665155	17:59:40.6	+66:51:55.7	0.02	0.03	0.200	0.037	0.197	0.037			
237	NEP175940+664028	17:59:40.7	+66:40:28.2	0.00	0.00	0.191	0.024	0.145	0.024			
238	NEP175942+662107	17:59:42.4	+66:21:08.0	0.12	0.09	0.150	0.030	0.165	0.032			
239	NEP175942+662722	17:59:42.7	+66:27:22.6	0.04	0.04	0.178	0.027	0.181	0.028			
240	NEP175943+662452	17:59:43.1	+66:24:52.7	0.11	0.15	0.133	0.022	0.126	0.024			

Table 1. continued.

Running number	Source name	RA	Dec	δRA	δDec	$S_{\rm peak}$	$S_{\rm peak}$ error	$S_{\rm total}$	$S_{\rm total}$ error	$\theta_{\rm maj}$	$\theta_{\rm min}$	PA
		hh:mm:ss.s	dd:mm:ss.s	$''$	$''$	mJy beam^{-1}	mJy beam^{-1}	mJy	mJy	$''$	$''$	$^\circ$
(1)	(2)	(3)	(4)	(5)	(6)	(7)	(8)	(9)	(10)	(11)	(12)	(13)
241	NEP175948+661457	17:59:48.3	+66:14:57.1	0.07	0.06	0.174	0.034	0.189	0.035			
242	NEP175953+664705	17:59:53.3	+66:47:05.3	0.02	0.02	0.828	0.030	0.880	0.042			
243	NEP175954+670218	17:59:55.0	+67:02:18.1	0.05	0.10	0.370	0.078	0.533	0.080	21.9		23.8
244	NEP175958+664647	17:59:59.0	+66:46:47.9	0.15	0.24	0.181	0.030	0.285	0.034	18.0	10.7	16.9
245	NEP175959+670249	17:59:59.1	+67:02:49.3	0.01	0.01	1.664	0.078	2.374	0.087	18.0	7.1	40.5
246	NEP18000+663110	18:00:0.2	+66:31:10.2	0.03	0.02	0.165	0.030	0.180	0.030			
247	NEP180002+661045	18:00:02.4	+66:10:45.8	0.04	0.02	0.269	0.042	0.243	0.043			
248	NEP180004+662257	18:00:04.8	+66:22:58.0	0.02	0.02	0.411	0.030	0.481	0.033			
249	NEP180005+661040	18:00:05.7	+66:10:41.0	0.03	0.41	0.385	0.042	0.111	0.042			
250	NEP180007+663654	18:00:07.1	+66:36:54.9	0.00	0.00	29.952	0.032	31.675	0.078			
251	NEP180008+664500	18:00:08.9	+66:45:00.6	0.33	0.30	0.148	0.034	0.364	0.037	26.0	18.6	49.3
252	NEP180010+661943	18:00:10.5	+66:19:43.5	0.01	0.01	3.339	0.032	5.475	0.103	17.2	11.6	–72.3
253	NEP180011+663326	18:00:11.3	+66:33:26.3	0.02	0.04	0.146	0.028	0.154	0.028			
254	NEP180011+665213	18:00:11.4	+66:52:13.6	0.15	0.33	0.450	0.032	0.743	0.051	22.6	5.0	16.3
255	NEP180016+662033	18:00:16.6	+66:20:33.3	0.06	0.05	0.174	0.032	0.218	0.033			
256	NEP180019+662404	18:00:19.6	+66:24:04.7	0.18	0.31	0.109	0.023	0.209	0.025	25.5	10.1	18.7
257	NEP180020+662226	18:00:20.3	+66:22:26.8	0.00	0.00	1.317	0.031	1.302	0.037			
258	NEP180021+670309	18:00:21.0	+67:03:09.9	0.00	0.00	0.795	0.076	0.789	0.076			
259	NEP180021+664212	18:00:21.7	+66:42:12.9	0.02	0.03	0.161	0.029	0.124	0.029			
260	NEP180022+663317	18:00:22.1	+66:33:17.1	0.00	0.00	0.235	0.028	0.173	0.028			
261	NEP180023+660515	18:00:23.3	+66:05:15.0	0.05	0.07	0.690	0.051	0.971	0.062			
262	NEP180023+661550	18:00:23.8	+66:15:50.0	0.05	0.32	0.172	0.031	0.293	0.034	31.0		0.3
263	NEP180027+665411	18:00:27.8	+66:54:11.3	0.00	0.00	4.833	0.049	5.551	0.054			
264	NEP180028+670552	18:00:28.7	+67:05:52.9	0.02	0.03	4.347	0.089	5.736	0.205			
265	NEP180028+664029	18:00:28.8	+66:40:29.3	0.00	0.00	2.586	0.029	2.511	0.034			
266	NEP180029+662920	18:00:29.4	+66:29:20.3	0.07	0.15	0.118	0.025	0.123	0.026			
267	NEP180030+670625	18:00:30.4	+67:06:25.0	0.04	0.22	0.458	0.089	0.610	0.091	22.4		3.3
268	NEP180031+670453	18:00:31.2	+67:04:53.5	0.01	0.02	0.557	0.076	0.620	0.077			
269	NEP180031+664411	18:00:31.3	+66:44:11.6	0.14	0.08	0.132	0.029	0.252	0.030	23.0	14.1	–83.0
270	NEP180032+661511	18:00:32.8	+66:15:11.8	0.01	0.02	0.248	0.037	0.179	0.037			
271	NEP180033+665248	18:00:33.0	+66:52:48.7	0.01	0.02	0.164	0.032	0.179	0.032			
272	NEP180033+664443	18:00:33.6	+66:44:43.1	0.00	0.00	8.407	0.034	9.596	0.092			
273	NEP180035+664941	18:00:35.6	+66:49:41.7	0.01	0.01	0.217	0.032	0.210	0.033			
274	NEP180035+662526	18:00:35.9	+66:25:26.1	0.01	0.02	0.176	0.023	0.083	0.024			
275	NEP180036+662207	18:00:36.4	+66:22:07.8	0.52	0.17	0.140	0.031	0.332	0.034	30.6	14.0	79.7
276	NEP180036+665221	18:00:36.6	+66:52:21.8	0.01	0.01	0.705	0.032	0.640	0.035			
277	NEP180037+664425	18:00:37.6	+66:44:26.0	0.01	0.01	6.044	0.026	7.509	0.167			
278	NEP180041+663355	18:00:41.7	+66:33:55.6	0.09	0.05	0.405	0.031	0.477	0.037			
279	NEP180042+664403	18:00:42.6	+66:44:03.4	0.71	0.41	0.109	0.026	0.249	0.027	26.5	16.8	85.2
280	NEP180047+661940	18:00:47.6	+66:19:40.3	0.02	0.02	0.751	0.035	0.856	0.045			

Table 1. continued.

Running number	Source name	RA	Dec	δRA	δDec	$S_{\rm peak}$	$S_{\rm peak}$ error	$S_{\rm total}$	$S_{\rm total}$ error	$\theta_{\rm maj}$	$\theta_{\rm min}$	PA
		hh:mm:ss.s	dd:mm:ss.s	$''$	$''$	mJy beam^{-1}	mJy beam^{-1}	mJy	mJy	$''$	$''$	$^\circ$
(1)	(2)	(3)	(4)	(5)	(6)	(7)	(8)	(9)	(10)	(11)	(12)	(13)
281	NEP180050+662927	18:00:50.9	+66:29:27.9	0.00	0.00	3.087	0.028	3.269	0.065			
282	NEP180053+663942	18:00:53.3	+66:39:42.5	0.01	0.01	0.194	0.029	0.103	0.029			
283	NEP180053+662302	18:00:53.9	+66:23:02.3	0.03	0.04	0.130	0.026	0.172	0.026	20.9		31.1
284	NEP180054+665443	18:00:54.6	+66:54:43.7	0.08	0.18	0.197	0.040	0.252	0.042	20.1		20.1
285	NEP180054+662955	18:00:54.6	+66:29:55.7	0.14	0.14	0.147	0.024	0.226	0.027			
286	NEP180056+664225	18:00:56.1	+66:42:25.3	0.01	0.03	0.172	0.026	0.148	0.026			
287	NEP180057+663722	18:00:57.4	+66:37:22.5	0.00	0.00	0.181	0.026	0.125	0.026			
288	NEP180057+661200	18:00:57.8	+66:12:00.1	0.02	0.02	0.373	0.036	0.308	0.037			
289	NEP180059+661057	18:00:59.6	+66:10:57.4	0.04	0.09	0.219	0.036	0.251	0.038			
290	NEP180059+662546	18:00:59.8	+66:25:46.2	0.07	0.12	0.124	0.027	0.195	0.028	21.1	7.7	–24.1
291	NEP180104+662738	18:01:04.3	+66:27:38.3	0.00	0.00	0.628	0.028	0.714	0.028			
292	NEP180104+663549	18:01:04.9	+66:35:50.0	0.01	0.01	0.259	0.026	0.220	0.026			
293	NEP180105+665812	18:01:05.1	+66:58:12.2	0.00	0.00	0.396	0.053	0.268	0.053			
294	NEP180105+664413	18:01:05.3	+66:44:13.4	0.27	0.20	0.123	0.026	0.285	0.027	26.9	16.5	–64.1
295	NEP180106+662753	18:01:06.4	+66:27:53.2	0.06	0.07	0.659	0.028	0.789	0.043			
296	NEP180106+664331	18:01:06.6	+66:43:31.5	0.01	0.06	0.276	0.102	0.103	0.102			
297	NEP180107+665910	18:01:07.3	+66:59:10.4	0.00	0.00	2.227	0.053	2.198	0.056			
298	NEP180108+664500	18:01:08.0	+66:45:00.4	0.22	0.15	0.754	0.050	3.346	0.088	36.0	29.7	–71.5
299	NEP180109+663331	18:01:09.1	+66:33:31.1	0.03	0.06	0.504	0.025	0.684	0.035	18.7		8.1
300	NEP180111+664022	18:01:11.4	+66:40:22.4	0.02	0.03	0.237	0.031	0.134	0.032			
301	NEP180114+663113	18:01:14.4	+66:31:13.3	0.00	0.00	3.979	0.032	4.242	0.049			
302	NEP180116+662404	18:01:16.3	+66:24:04.4	0.07	0.24	0.171	0.027	0.176	0.030			
303	NEP180119+663401	18:01:19.4	+66:34:01.9	0.01	0.01	0.226	0.025	0.184	0.025			
304	NEP180120+663722	18:01:20.5	+66:37:22.1	0.01	0.02	0.207	0.025	0.144	0.025			
305	NEP180121+663031	18:01:21.2	+66:30:31.6	0.10	0.03	0.443	0.032	1.125	0.040	32.3	14.4	84.8
306	NEP180121+671850	18:01:21.3	+67:18:50.9	0.03	0.19	5.970	0.357	10.128	0.449	23.9	5.4	7.5
307	NEP180123+664346	18:01:23.8	+66:43:46.3	0.02	0.01	12.286	0.102	18.249	0.460			
308	NEP180127+664020	18:01:27.4	+66:40:20.7	0.00	0.01	0.511	0.031	0.363	0.032			
309	NEP180127+670054	18:01:27.7	+67:00:54.1	0.03	0.04	0.489	0.061	0.708	0.063	19.4	6.5	–26.3
310	NEP180128+662854	18:01:28.2	+66:28:54.1	0.01	0.01	0.667	0.031	0.722	0.034			
311	NEP180128+671109	18:01:28.9	+67:11:09.1	0.07	0.12	0.939	0.194	1.322	0.202	18.7	5.7	9.5
312	NEP180133+664449	18:01:33.2	+66:44:49.7	0.06	0.04	1.480	0.050	6.430	0.095	37.3	27.7	85.8
313	NEP180133+665640	18:01:33.5	+66:56:41.0	0.05	0.09	0.736	0.054	0.951	0.069			
314	NEP180142+660416	18:01:42.1	+66:04:16.4	0.01	0.02	0.361	0.065	0.276	0.065			
315	NEP180143+664108	18:01:43.0	+66:41:08.5	0.00	0.00	1.559	0.028	1.488	0.030			
316	NEP180143+665252	18:01:43.7	+66:52:52.5	0.00	0.00	1.026	0.037	1.037	0.039			
317	NEP180143+664521	18:01:44.0	+66:45:21.2	0.01	0.02	0.149	0.028	0.151	0.028			
318	NEP180144+664137	18:01:44.5	+66:41:37.6	0.00	0.00	0.339	0.031	0.264	0.031			
319	NEP180146+661609	18:01:46.1	+66:16:010.0	0.01	0.01	0.241	0.033	0.158	0.033			
320	NEP180146+663840	18:01:46.8	+66:38:40.5	0.00	0.00	1.436	0.028	1.419	0.035			

Table 1. continued.

Running number (1)	Source name (2)	RA hh:mm:ss.s (3)	Dec dd:mm:ss.s (4)	δRA $''$ (5)	δDec $''$ (6)	$S_{\rm peak}$ mJy beam^{-1} (7)	$S_{\rm peak}$ error mJy beam^{-1} (8)	$S_{\rm total}$ mJy (9)	$S_{\rm total}$ error mJy (10)	$\theta_{\rm maj}$ $''$ (11)	$\theta_{\rm min}$ $''$ (12)	PA $^\circ$ (13)
321	NEP180148+661438	18:01:48.6	+66:14:39.0	0.00	0.00	0.623	0.039	0.554	0.039			
322	NEP180148+670146	18:01:49.0	+67:01:46.6	0.01	0.03	0.866	0.057	1.045	0.064			
323	NEP180149+665912	18:01:49.2	+66:59:12.3	0.01	0.01	0.511	0.057	0.391	0.057			
324	NEP180149+665130	18:01:49.7	+66:51:30.6	0.02	0.03	0.262	0.037	0.253	0.038			
325	NEP180151+663424	18:01:51.2	+66:34:24.4	0.00	0.00	0.330	0.027	0.222	0.027			
326	NEP180152+664557	18:01:52.4	+66:45:57.3	0.00	0.01	0.554	0.028	0.487	0.029			
327	NEP180153+670608	18:01:53.7	+67:06:08.9	0.00	0.00	3.660	0.115	4.192	0.120			
328	NEP180154+661859	18:01:54.6	+66:18:59.5	0.01	0.01	0.163	0.029	0.126	0.029			
329	NEP180157+665717	18:01:57.7	+66:57:17.5	0.02	0.02	6.969	0.106	10.952	0.260	18.5	8.3	40.7
330	NEP180158+670732	18:01:58.7	+67:07:32.3	0.10	0.64	0.518	0.115	1.928	0.122	47.6	15.9	–5.1
331	NEP18020+662526	18:02:0.3	+66:25:26.3	0.02	0.02	0.157	0.027	0.126	0.027			
332	NEP18020+663351	18:02:0.6	+66:33:51.4	0.06	0.05	0.139	0.027	0.139	0.028			
333	NEP180201+661647	18:02:01.3	+66:16:47.4	0.06	0.08	0.368	0.033	0.423	0.038			
334	NEP180204+665755	18:02:04.4	+66:57:55.9	0.00	0.00	11.014	0.106	15.851	0.205			
335	NEP180206+662608	18:02:06.0	+66:26:08.5	0.03	0.04	0.404	0.028	0.428	0.032			
336	NEP180208+661748	18:02:08.5	+66:17:48.1	0.01	0.01	0.515	0.037	0.469	0.039			
337	NEP180216+664330	18:02:16.0	+66:43:30.0	0.02	0.02	0.282	0.035	0.315	0.036			
338	NEP180216+661903	18:02:17.0	+66:19:03.9	0.02	0.04	0.170	0.036	0.302	0.036	23.0	11.1	–16.7
339	NEP180221+660032	18:02:21.4	+66:00:32.4	0.00	0.01	4.310	0.097	5.088	0.128			
340	NEP180223+671026	18:02:23.6	+67:10:26.2	0.03	0.06	3.491	0.140	6.111	0.223	23.1	7.4	17.4
341	NEP180226+664105	18:02:26.9	+66:41:05.8	0.01	0.01	0.462	0.031	0.426	0.032			
342	NEP180229+664018	18:02:29.3	+66:40:18.9	0.05	0.05	0.194	0.031	0.171	0.033			
343	NEP180230+660937	18:02:30.1	+66:09:37.8	0.06	0.04	0.337	0.049	0.252	0.051			
344	NEP180232+665128	18:02:32.2	+66:51:28.2	0.00	0.01	0.367	0.039	0.259	0.039			
345	NEP180238+665536	18:02:38.7	+66:55:36.4	0.00	0.00	0.455	0.047	0.426	0.049			
346	NEP180242+662349	18:02:42.8	+66:23:49.7	0.01	0.02	0.432	0.039	0.435	0.040			
347	NEP180245+664158	18:02:45.6	+66:41:58.8	0.00	0.00	0.520	0.035	0.420	0.036			
348	NEP180246+655144	18:02:46.7	+65:51:44.3	6.36	0.93	1.037	0.249	2.025	0.280	34.1	2.7	69.7
349	NEP180246+664815	18:02:46.7	+66:48:15.1	0.00	0.00	4.342	0.040	4.734	0.045			
350	NEP180247+670015	18:02:47.9	+67:00:15.2	0.18	0.36	0.280	0.064	0.576	0.069	27.1	11.0	–19.0
351	NEP180249+665106	18:02:49.4	+66:51:06.8	0.00	0.01	0.273	0.040	0.246	0.040			
352	NEP180252+670409	18:02:52.4	+67:04:09.5	0.06	0.04	0.453	0.086	0.374	0.088			
353	NEP180252+662055	18:02:52.7	+66:20:55.8	0.02	0.05	0.229	0.041	0.165	0.042			
354	NEP180253+665131	18:02:53.2	+66:51:31.9	0.00	0.01	0.302	0.040	0.232	0.040			
355	NEP180253+670331	18:02:53.6	+67:03:31.9	0.40	0.15	0.398	0.086	0.582	0.091	21.4	5.5	67.1
356	NEP180256+662232	18:02:56.9	+66:22:32.4	0.05	0.05	0.211	0.039	0.145	0.040			
357	NEP180258+662811	18:02:58.6	+66:28:11.2	0.00	0.00	0.268	0.030	0.163	0.030			
358	NEP18030+660412	18:03:0.3	+66:04:12.4	0.03	0.02	0.532	0.084	0.437	0.085			
359	NEP180301+662353	18:03:01.2	+66:23:53.1	0.00	0.00	2.519	0.039	2.611	0.046			
360	NEP180304+663634	18:03:04.7	+66:36:35.0	0.07	0.09	0.190	0.031	0.210	0.033			

Table 1. continued.

Running number	Source name	RA	Dec	δRA	δDec	$S_{\rm peak}$	$S_{\rm peak}$ error	$S_{\rm total}$	$S_{\rm total}$ error	$\theta_{\rm maj}$	$\theta_{\rm min}$	PA
		hh:mm:ss.s	dd:mm:ss.s	$''$	$''$	mJy beam^{-1}	mJy beam^{-1}	mJy	mJy	$''$	$''$	$^\circ$
(1)	(2)	(3)	(4)	(5)	(6)	(7)	(8)	(9)	(10)	(11)	(12)	(13)
361	NEP180311+663848	18:03:11.3	+66:38:48.8	0.00	0.00	1.122	0.046	1.049	0.048			
362	NEP180311+661408	18:03:11.8	+66:14:08.2	0.13	0.18	0.259	0.052	0.288	0.054			
363	NEP180312+660147	18:03:12.3	+66:01:48.0	0.03	0.04	0.871	0.128	1.274	0.132	17.7	9.5	–35.5
364	NEP180312+662030	18:03:12.8	+66:20:30.4	0.05	0.06	0.234	0.041	0.162	0.042			
365	NEP180314+655423	18:03:14.4	+65:54:23.8	0.01	0.02	5.138	0.333	6.956	0.361	17.9	4.1	–25.7
366	NEP180316+664226	18:03:16.3	+66:42:26.5	0.00	0.00	8.307	0.052	8.565	0.081			
367	NEP180321+663052	18:03:21.4	+66:30:52.2	0.01	0.01	0.247	0.041	0.169	0.041			
368	NEP180328+664108	18:03:28.7	+66:41:08.9	0.01	0.01	0.581	0.046	0.671	0.048			
369	NEP180329+664707	18:03:29.2	+66:47:07.3	0.19	0.25	0.231	0.038	0.405	0.041	21.4	11.5	–41.4
370	NEP180330+661512	18:03:30.1	+66:15:13.0	0.04	0.05	0.246	0.045	0.196	0.046			
371	NEP180331+662112	18:03:31.4	+66:21:12.6	0.00	0.00	0.468	0.042	0.389	0.042			
372	NEP180334+662033	18:03:34.8	+66:20:33.9	0.02	0.01	0.300	0.051	0.270	0.051			
373	NEP180341+670310	18:03:41.7	+67:03:10.4	0.19	0.30	0.530	0.134	2.483	0.144	38.4	31.4	3.3
374	NEP180346+662054	18:03:46.6	+66:20:54.3	0.01	0.01	0.733	0.051	0.623	0.053			
375	NEP180346+660927	18:03:46.9	+66:09:27.8	0.01	0.01	0.837	0.078	0.777	0.079			
376	NEP180347+663437	18:03:47.9	+66:34:37.4	0.02	0.02	0.212	0.033	0.131	0.034			
377	NEP180348+660540	18:03:49.0	+66:05:40.8	0.01	0.02	9.358	0.154	13.784	0.205	18.8	6.4	–33.3
378	NEP180351+660516	18:03:51.2	+66:05:16.8	0.00	0.01	27.202	0.154	41.616	0.611	20.4		–25.9
379	NEP180352+655531	18:03:52.9	+65:55:31.5	0.00	0.00	1.155	0.225	1.074	0.235			
380	NEP180355+662034	18:03:55.5	+66:20:34.8	0.16	0.21	0.217	0.051	0.470	0.054	28.3	12.5	–36.8
381	NEP180357+662735	18:03:57.7	+66:27:35.0	0.03	0.05	0.286	0.043	0.274	0.045			
382	NEP18040+662836	18:04:0.3	+66:28:36.8	0.06	0.03	0.279	0.043	0.264	0.045			
383	NEP18040+663525	18:04:0.9	+66:35:25.6	0.06	0.05	0.695	0.033	0.989	0.051			
384	NEP180403+671318	18:04:03.8	+67:13:18.3	0.05	0.07	1.553	0.283	1.356	0.292			
385	NEP180407+671402	18:04:08.0	+67:14:02.4	0.04	0.08	3.657	0.491	7.951	0.527	28.0	12.0	–4.8
386	NEP180408+664426	18:04:08.4	+66:44:26.2	0.01	0.01	0.556	0.050	0.518	0.051			
387	NEP180410+655149	18:04:10.4	+65:51:49.6	0.11	0.27	2.039	0.468	2.605	0.489	19.1		26.7
388	NEP180410+662723	18:04:10.5	+66:27:23.3	0.06	0.06	0.826	0.053	1.476	0.068	25.3	7.1	44.9
389	NEP180410+665712	18:04:10.7	+66:57:12.1	0.05	0.10	2.492	0.092	5.091	0.114	24.5	12.6	11.7
390	NEP180411+665737	18:04:11.7	+66:57:37.7	0.05	0.41	3.504	0.092	9.991	0.296	41.8	7.2	9.6
391	NEP180422+660021	18:04:22.2	+66:00:21.0	0.03	0.02	1.153	0.173	0.951	0.178			
392	NEP180422+664132	18:04:23.0	+66:41:32.2	0.04	0.04	0.267	0.047	0.210	0.048			
393	NEP180425+664627	18:04:26.0	+66:46:27.4	0.09	0.08	0.313	0.050	0.292	0.053			
394	NEP180426+662244	18:04:26.5	+66:22:44.3	0.04	0.04	0.320	0.053	0.383	0.055			
395	NEP180427+662403	18:04:27.5	+66:24:03.5	0.42	0.26	0.249	0.049	0.396	0.055	19.8	10.3	–70.8
396	NEP180435+662707	18:04:35.9	+66:27:07.6	0.00	0.00	6.454	0.061	6.697	0.084			
397	NEP180436+662531	18:04:36.8	+66:25:32.0	0.00	0.00	73.613	0.144	77.644	0.394			
398	NEP180438+660500	18:04:38.9	+66:05:00.0	0.00	0.00	3.474	0.175	4.146	0.182			
399	NEP180453+664021	18:04:53.5	+66:40:21.9	0.03	0.02	0.276	0.052	0.281	0.054			
400	NEP180455+665251	18:04:55.2	+66:52:51.9	8.26	8.40	0.719	0.079	0.275	0.079			

Table 1. continued.

Running number	Source name	RA	Dec	δRA	δDec	$S_{\rm peak}$	$S_{\rm peak}$ error	$S_{\rm total}$	$S_{\rm total}$ error	$\theta_{\rm maj}$	$\theta_{\rm min}$	PA
		hh:mm:ss.s	dd:mm:ss.s	$''$	$''$	mJy beam^{-1}	mJy beam^{-1}	mJy	mJy	$''$	$''$	$^\circ$
(1)	(2)	(3)	(4)	(5)	(6)	(7)	(8)	(9)	(10)	(11)	(12)	(13)
401	NEP180456+664633	18:04:56.2	+66:46:33.5	0.14	0.14	0.252	0.057	0.357	0.059			
402	NEP180456+663106	18:04:56.3	+66:31:06.5	0.09	0.07	0.310	0.060	0.462	0.061	19.3	8.7	–51.9
403	NEP180457+665351	18:04:57.8	+66:53:51.5	0.02	0.02	16.561	0.787	34.084	0.972	21.0	16.5	26.1
404	NEP180458+665700	18:04:58.1	+66:57:00.8	0.01	0.02	8.422	0.109	18.625	0.328	23.6	14.7	–0.1
405	NEP180501+663050	18:05:01.2	+66:30:50.7	0.11	0.17	0.780	0.060	0.985	0.086			
406	NEP180502+665318	18:05:02.8	+66:53:18.6	0.00	0.00	28.016	0.787	39.701	0.909			
407	NEP180507+663132	18:05:07.8	+66:31:32.7	0.08	0.15	0.259	0.054	0.396	0.056	19.9	7.8	3.6
408	NEP180508+663239	18:05:08.3	+66:32:39.2	0.25	0.21	0.323	0.066	0.548	0.072	23.3	8.7	–54.2
409	NEP180509+664533	18:05:09.2	+66:45:33.6	0.17	0.25	0.313	0.073	0.738	0.076	31.3	12.9	–33.6
410	NEP180512+661957	18:05:12.5	+66:19:57.7	0.01	0.01	0.607	0.095	0.472	0.096			
411	NEP180514+665643	18:05:14.6	+66:56:43.7	0.01	0.01	1.463	0.137	1.459	0.140			
412	NEP180516+662111	18:05:16.0	+66:21:11.6	0.01	0.01	5.583	0.078	9.464	0.166	19.9	9.6	16.2
413	NEP180517+665403	18:05:17.2	+66:54:03.6	0.01	0.01	1.475	0.109	1.554	0.114			
414	NEP180517+664451	18:05:17.7	+66:44:51.0	0.01	0.04	2.189	0.073	3.707	0.114	22.9	5.9	–2.4
415	NEP180518+663512	18:05:18.2	+66:35:12.4	0.00	0.00	1.423	0.066	1.500	0.070			
416	NEP180526+662105	18:05:26.6	+66:21:05.2	0.08	0.06	0.444	0.078	0.664	0.082			
417	NEP180527+663946	18:05:27.8	+66:39:46.6	0.05	0.03	0.362	0.062	0.310	0.063			
418	NEP180530+664451	18:05:30.9	+66:44:51.5	0.01	0.01	1.928	0.073	2.299	0.084			
419	NEP180531+671009	18:05:31.1	+67:10:09.4	0.01	0.01	16.566	0.436	36.497	0.598	24.0	15.8	34.3
420	NEP180532+661803	18:05:32.8	+66:18:03.3	0.03	0.02	2.348	0.103	3.420	0.138	19.9	5.2	–58.4
421	NEP180538+664157	18:05:38.5	+66:41:57.4	0.00	0.00	1.383	0.083	1.327	0.084			
422	NEP180541+664239	18:05:41.4	+66:42:39.8	0.09	0.04	0.401	0.083	0.502	0.085			
423	NEP180541+665002	18:05:41.7	+66:50:02.8	0.01	0.02	0.932	0.121	0.972	0.122			
424	NEP180545+662125	18:05:45.2	+66:21:25.4	0.05	0.05	0.477	0.078	0.413	0.081			
425	NEP180545+660331	18:05:45.4	+66:03:31.0	0.15	0.07	1.288	0.255	1.033	0.263			
426	NEP180545+662611	18:05:45.4	+66:26:11.6	0.00	0.00	4.383	0.079	4.748	0.089			
427	NEP180554+664525	18:05:54.1	+66:45:25.1	0.01	0.01	6.323	0.093	8.993	0.156			
428	NEP180556+663056	18:05:56.3	+66:30:56.2	0.00	0.00	8.669	0.075	10.389	0.128			
429	NEP180557+662954	18:05:57.7	+66:29:54.8	0.00	0.00	3.768	0.075	4.436	0.091			
430	NEP180557+664509	18:05:57.8	+66:45:09.5	0.01	0.01	9.320	0.093	12.653	0.262			
431	NEP180558+665503	18:05:58.5	+66:55:03.4	0.01	0.01	3.902	0.123	5.289	0.147			
432	NEP180618+662754	18:06:18.0	+66:27:54.8	0.03	0.16	0.457	0.083	0.447	0.086			
433	NEP180619+664024	18:06:19.6	+66:40:24.2	0.35	0.22	0.360	0.080	0.618	0.084	25.9	6.9	–60.5
434	NEP180620+663006	18:06:20.9	+66:30:06.2	0.30	4.99	1.001	0.090	2.792	0.175	44.4	3.7	–2.5
435	NEP180621+665121	18:06:21.5	+66:51:21.1	0.13	0.10	0.641	0.135	0.709	0.140			
436	NEP180625+661958	18:06:25.6	+66:19:58.2	0.02	0.01	1.417	0.141	1.921	0.145			
437	NEP180637+662203	18:06:37.9	+66:22:03.1	0.10	0.88	0.598	0.145	2.044	0.157	53.5	8.5	–1.5
438	NEP180639+663243	18:06:39.5	+66:32:43.1	0.00	0.00	1.268	0.130	1.394	0.131			
439	NEP180642+662654	18:06:42.5	+66:26:54.1	0.11	6.02	0.501	0.130	2.253	0.144	91.3		2.9
440	NEP180646+662738	18:06:46.9	+66:27:38.2	0.00	0.00	7.998	0.130	8.760	0.147			

Table 1. continued.

Running number	Source name	RA	Dec	δRA	δDec	$S_{\rm peak}$	$S_{\rm peak}$ error	$S_{\rm total}$	$S_{\rm total}$ error	$\theta_{\rm maj}$	$\theta_{\rm min}$	PA
		hh:mm:ss.s	dd:mm:ss.s	$''$	$''$	mJy beam^{-1}	mJy beam^{-1}	mJy	mJy	$''$	$''$	$^\circ$
(1)	(2)	(3)	(4)	(5)	(6)	(7)	(8)	(9)	(10)	(11)	(12)	(13)
441	NEP180648+665041	18:06:48.5	+66:50:41.8	0.03	0.06	1.178	0.214	1.257	0.219			
442	NEP18070+665648	18:07:0.6	+66:56:48.5	0.51	0.08	1.155	0.256	1.956	0.270	27.3	5.6	89.6
443	NEP180701+664700	18:07:01.0	+66:47:00.4	0.01	0.01	1.738	0.138	1.831	0.142			
444	NEP180703+670115	18:07:03.3	+67:01:15.6	0.12	0.17	1.901	0.378	2.904	0.398	18.1	10.0	–8.6
445	NEP180704+662807	18:07:04.5	+66:28:07.8	0.03	0.03	6.598	0.160	10.341	0.343			
446	NEP180714+660732	18:07:14.9	+66:07:32.0	0.04	0.11	3.046	0.513	1.945	0.536			
447	NEP180719+661847	18:07:19.0	+66:18:47.1	0.11	0.34	6.731	0.232	17.190	0.791	30.4	13.0	–5.5
448	NEP180720+661452	18:07:20.2	+66:14:52.9	0.19	0.29	1.132	0.239	1.627	0.254	20.6	3.8	–34.1
449	NEP180722+662306	18:07:22.9	+66:23:06.3	0.04	0.03	1.483	0.180	2.155	0.186			
450	NEP180729+662836	18:07:29.6	+66:28:36.6	0.03	0.05	3.280	0.201	8.399	0.245	32.6	13.5	32.1
451	NEP180736+665755	18:07:36.1	+66:57:55.0	0.25	0.16	2.080	0.453	3.095	0.470	19.8	8.1	56.3
452	NEP180741+663725	18:07:41.7	+66:37:25.8	0.03	0.02	1.696	0.205	2.115	0.209			
453	NEP180750+663130	18:07:50.7	+66:31:30.6	0.04	0.08	1.311	0.242	1.072	0.248			
454	NEP180751+662400	18:07:51.8	+66:24:00.2	0.15	0.16	1.181	0.217	1.370	0.235			
455	NEP180752+661737	18:07:52.9	+66:17:37.6	0.01	0.01	12.760	0.325	18.159	0.454			
456	NEP180757+662852	18:07:58.0	+66:28:53.0	0.24	1.78	0.896	0.201	1.933	0.219	44.1		–10.7
457	NEP180823+663709	18:08:24.0	+66:37:09.4	0.10	0.42	1.153	0.272	2.601	0.284	35.4	6.7	17.7
458	NEP180829+663840	18:08:30.0	+66:38:40.3	0.05	0.13	1.723	0.298	1.280	0.313			
459	NEP180849+663434	18:08:49.1	+66:34:34.8	0.00	0.00	13.220	0.436	18.334	0.483			
460	NEP180855+664617	18:08:55.4	+66:46:17.7	0.51	0.92	2.688	0.522	4.104	0.554	21.1	5.3	0.8
461	NEP180859+663059	18:08:59.4	+66:30:59.5	0.04	0.01	4.409	0.498	5.925	0.512	20.3	3.9	–86.2
462	NEP180910+663849	18:09:11.0	+66:38:49.5	0.44	0.51	2.607	0.602	4.774	0.666	19.9	14.6	–61.4